Journal of Geodesy (2020) 94:115
https://doi.org/10.1007/s00190-020-01445-w

ORIGINAL ARTICLE

Atmospheric pressure loading in GPS positions: dependency on GPS processing methods and effect on assessment of seasonal deformation in the contiguous USA and Alaska

Hilary R. Martens[1] · Donald F. Argus[2] · Cody Norberg[3] · Geoffrey Blewitt[4] · Thomas A. Herring[5] · Angelyn W. Moore[2] · William C. Hammond[4] · Corné Kreemer[4]

Received: 10 April 2020 / Accepted: 29 September 2020 / Published online: 18 November 2020

Abstract
The Global Positioning System (GPS) has revolutionized the ability to monitor Earth-system processes, including Earth's water cycle. Several analysis centers process GPS data to estimate ground-antenna positions at daily temporal resolution. Differences in processing strategies can lead to inconsistencies in coordinate-position estimates and therefore influence the analysis of crustal displacement associated with variations in atmospheric and hydrologic mass loading. Here, we compare five GPS data products produced by three processing centers: the Nevada Geodetic Laboratory, Jet Propulsion Laboratory, and UNAVCO Consortium. We find that 5 to 30% of the scatter in residual GPS time series (commonly considered noise) can be explained by atmospheric loading in the contiguous USA and Alaska, but that the percentages vary widely by data product. Positions derived using high-resolution troposphere models (e.g., ECMWF) exhibit significantly lower scatter after correcting for atmospheric loading than positions estimated using constant or slowly varying troposphere models (e.g., GPT2w). The data products also exhibit differences in seasonal deformation (commonly attributed, in large part, to fluctuations in hydrologic mass loading): median vector differences in estimated seasonal amplitude range from 0.4–1.0 mm in the vertical component and 0.1–0.3 mm in the horizontal components, or about 10–40% of the mean amplitudes of seasonal oscillation. Newer products exhibit lower total scatter and stronger correlations than older products. Network-coherent differences in estimates of seasonal deformation reveal reference-frame inconsistencies between data products. We also cross-check two independent models of atmospheric pressure loading: ESMGFZ and LoadDef.

Keywords Elastic Earth deformation · Atmospheric pressure loading · Troposphere delays · GPS processing · GNSS processing · Hydrologic loading · Seasonal Earth deformation

1 Introduction

The Global Positioning System (GPS) records displacements of Earth's surface associated with a variety of natural processes, including tectonic and volcanic deformation, earthquake offsets and relaxation, glacial isostatic adjustment, the redistribution of oceanic and atmospheric mass, and variations in continental water storage. The precise processing of the raw satellite data recorded by ground-based receivers is critical to quantifying and interpreting Earth-system processes; however, processing strategies are complex and involve many assumptions and tunable parameters. Furthermore, some of the geophysical signals exhibit similar temporal and spatial patterns, which requires additional analysis at the post-processing stage to decompose the time series into its component parts.

✉ Hilary R. Martens
hilary.martens@umontana.edu

1 Department of Geosciences, University of Montana, Missoula, USA

2 Jet Propulsion Laboratory, California Institute of Technology, Pasadena, USA

3 Department of Physics and Astronomy, University of Montana, Missoula, USA

4 Nevada Geodetic Laboratory, Nevada Bureau of Mines and Geology, University of Nevada, Reno, USA

5 Department of Earth, Atmospheric, and Planetary Sciences, Massachusetts Institute of Technology, Cambridge, USA

An emerging sub-field of geodesy, called hydrogeodesy, uses GPS and other geodetic datasets to advance understanding of the Earth's hydrological cycle. Although large variations in hydrologic mass occur predominantly at seasonal timescales (e.g., Argus et al. 2014; Borsa et al. 2014; Fu et al. 2015; Argus et al. 2017), short-period transient variations in hydrologic mass can also manifest due to, for example, individual episodes of intense precipitation and runoff (e.g., Milliner et al. 2018; Springer et al. 2019). In order to best characterize crustal deformation caused by the redistribution of water mass across a broad range of timescales, other known sources of deformation must be modeled and removed from the GPS time series.

One of the most prominent sources of crustal deformation recorded by GPS arises from variations in atmospheric surface pressure, which fluctuates predominantly on timescales of hours to weeks as well as at annual (i.e., one-year) periods (e.g., van Dam et al. 1994, 1997; Wijaya et al. 2013). Solid Earth's elastic response to the redistribution of atmospheric mass each day can exceed 10 mm (e.g., Petrov and Boy 2004; Williams and Penna 2011; Dill and Dobslaw 2013), which is similar to the scale of deformation associated with hydrologic mass loading (e.g., Fu et al. 2015; Argus et al. 2017).

To accommodate a wide array of possible scientific applications that take advantage of GPS observations of crustal deformation, to prioritize other processing needs, and in adherence to IERS conventions (Petit and Luzum 2010), atmospheric pressure loading is not routinely modeled and removed from GPS data during processing (e.g., Williams and Penna 2011; Männel et al. 2019; Mémin et al. 2020). Thus, it is the responsibility of the end user to make appropriate corrections for atmospheric loading if necessary. To facilitate the corrections, predictions of surface deformation caused by fluctuations in atmospheric surface pressure are now regularly computed based on numerical weather models informed by empirical data, and made available on global grids at high (sub-daily) temporal resolution (e.g., Petrov and Boy 2004; Dill and Dobslaw 2013; Wijaya et al. 2013).

Prior studies have shown, however, that the methods used to process GPS data can significantly impact the retention of atmospheric-loading signals in the position time series (e.g., Tregoning and Herring 2006; Kouba 2009; Steigenberger et al. 2009; Tregoning and Watson 2009, 2011). In particular, mismodeling the travel-time delays of GPS signals through the troposphere can result in increased position errors and a partial compensation of atmospheric pressure loading (e.g., Tregoning and Herring 2006; Steigenberger et al. 2009). Vertical position estimates are negatively correlated with troposphere delay (Steigenberger et al. 2009): thus, it is easy to absorb mismodeled troposphere delay into estimates of GPS height changes caused by atmospheric pressure loading. An increase in atmospheric pressure produces an increase in the zenith delay and a downward displacement of the GPS; similarly, a decrease in atmospheric pressure produces a decrease in the zenith delay and an upward displacement of the GPS. When the zenith delay is underestimated relative to the true pressure conditions, the displacement of the GPS due to atmospheric pressure loading can also be underestimated relative to the true surface deflection.

Height errors of up to 10 mm in polar regions can result when inaccurate (e.g., static or slowly varying) values for zenith hydrostatic delays are used during GPS processing, particularly if low satellite elevation-angle cutoffs are also used and if corrections to the a priori zenith delays are estimated using only wet mapping functions (Boehm et al. 2006a; Tregoning and Herring 2006; Kouba 2009). Furthermore, Steigenberger et al. (2009) found that seasonal fluctuations in station height can vary by up to about 1 mm depending on the troposphere-delay models used during processing. As a result, correcting for atmospheric loading at the post-processing stage using high-resolution models can run the risk of overcorrecting for atmospheric loading when oversimplified or mismodeled troposphere delays are used during initial processing.

Although high-resolution (temporal and spatial) troposphere delays derived from numerical weather models consistently yield the most accurate GPS position estimates, and prior studies have recommended against using approximate, low-resolution troposphere delays during GPS processing (e.g., Kouba 2009; Steigenberger et al. 2009; Munekane and Boehm 2010), some contemporary and widely available GPS data products have utilized static or slowly varying a priori troposphere-delay models during processing (so-called blind models) for reasons of convenience and practicality, such as ease of implementation and availability of models at low latency (e.g., Boehm et al. 2006a, 2015). Since imprecise GPS coordinate positions can influence assessments of surface mass loading, including critical estimates of freshwater storage and movement, we aim to quantify the discrepancies in GPS positions among several key datasets and examine the practical effects of their differences on signatures of water-mass loading across the spatially dense Plate Boundary Observatory (PBO) network (now superseded by the Network of the Americas, NOTA) in the contiguous USA and Alaska.

The main objectives and outcomes of our study include: (1) assessing the extent to which atmospheric pressure loading can explain scatter in three-component (east, north, up) residual time series across the contiguous USA and Alaska at high spatial resolution; (2) comparing time-series scatter when correcting for atmospheric loading for five GPS data products generated by three independent processing centers employing two independent software packages; and (3) evaluating the effects of GPS processing and atmospheric-loading corrections on estimates of three-component annual deformation, which is largely associated with seasonal

changes in continental water storage. Discrepancies between data products can place bounds on the observational precision of inferred seasonal water-storage variations. We interpret the discrepancies in the context of individual time-series precision, which has improved with newer data-processing methods. We also consider best practices for treating atmospheric pressure loading in GPS time series.

2 Methods

2.1 GPS data processing and product comparisons

We investigate five GPS data products: a recent re-analysis by the Nevada Geodetic Laboratory ("NGL-IGS14") (Blewitt et al. 2018); a former analysis by the Nevada Geodetic Laboratory ("NGL-IGS08"); a recent re-analysis by the Jet Propulsion Laboratory ("JPL-2018a") (Zumberge et al. 1997; Bertiger et al. 2020; Heflin et al. 2020); a former analysis by the Jet Propulsion Laboratory ("JPL-2011b"); and a recent (pre-September 2019) analysis by the UNAVCO consortium ("UNAVCO") (Herring et al. 2016). The position estimates produced by the UNAVCO Consortium reflect the combined solutions from two processing centers: Central Washington University (CWU) and New Mexico Tech (NMT). We analyze a total of 1832 GPS sites in North America, mostly from the PBO and GAGE networks, over the three-year period from October 2012 to October 2015. We focus on the 1185 GPS sites that are common to all five products for statistical analyses, and show all available stations for each product in select map-view figures (see captions).

Two of the most widely used software packages for processing GPS data are GIPSY-OASIS (now superseded by GipsyX) (Zumberge et al. 1997; Bertiger et al. 2020) and GAMIT/GLOBK (Herring et al. 2016). Both GIPSY and GipsyX use a precise point positioning (PPP) algorithm based on a filtering approach to estimate the position coordinates of a single GPS receiver (Zumberge et al. 1997; Bertiger et al. 2010, 2020). GAMIT adopts a double-difference approach to estimate the positions of multiple stations within a network (e.g., Dong et al. 1998; Herring et al. 2016). Both NGL and JPL use the GIPSY/GipsyX software exclusively; UNAVCO generates combined solutions from GIPSY and GAMIT (Herring et al. 2016). NGL-IGS14 and JPL-2018a use GipsyX and its IGS14 products, whereas NGL-IGS08 and JPL-2011b use GIPSY v6 and its IGS08 products. UNAVCO uses GIPSY v6 with JPL-generated orbit and clock products in the IGS08 frame combined with GAMIT/GLOBK using IGS08 orbit products. (Clock products are not needed for GAMIT/GLOBK.) For the height time series, UNAVCO products are dominated by the CWU GIPSY v6 contribution (Herring et al. 2016).

One of the most challenging aspects of GPS data processing, which is important to both approaches for antenna-position estimation, involves the treatment of radio-signal propagation delays through the Earth's troposphere. Troposphere-delay models characterize the influence of atmospheric density and water-vapor content on the transmission speed of GPS signals from satellite to receiver relative to a vacuum. The greater the density and water-vapor content of the air column through which a GPS signal propagates, the greater the delay of the signal. Troposphere delays depend on the angle of transmission through the atmosphere: satellite signals traveling closer to the horizon must propagate through a longer atmospheric air column, which increases the delay. In GPS processing, estimates of hydrostatic and wet troposphere delays are generally made for a vertical column of air directly above the station (at zenith), and empirical functions are used to map the delays at zenith to lower angles of atmospheric transmission.

The troposphere delays, when mismodeled, can translate directly into an incorrect estimate of the satellite-to-antenna distance and affect GPS inferences of ground displacements associated with atmospheric loading (e.g., Tregoning and Herring 2006; Kouba 2009; Steigenberger et al. 2009). Different methods and models exist to account for the troposphere delays. Commonly, the zenith hydrostatic delays, and sometimes also the zenith wet delays, are given by numerical weather models (e.g., Simmons et al. 2007), and empirical functions are used to map the zenith delays to lower satellite elevations relative to the horizon (e.g., Boehm et al. 2006a, b). Nominal values for the hydrostatic and wet components of the delay at zenith are about 2 m and 0.1–0.4 m, respectively (e.g., Niell 1996). Although the wet component of the delay accounts for a smaller percentage of the total troposphere delay, the wet component exhibits larger fluctuations with time (e.g., Bevis et al. 1992; Tregoning and Herring 2006; Jin et al. 2014).

Of the data products considered here, three use numerical weather models based on empirical data at high temporal resolution (i.e., daily or sub-daily) to characterize the a priori zenith hydrostatic and wet delays and tropospheric mapping functions: NGL-IGS14, UNAVCO, and JPL-2011b. In each case, the models are derived from the European Centre for Medium-Range Weather Forecasts (ECMWF) and the Vienna Mapping Functions (VMF1) (Boehm et al. 2006b; Simmons et al. 2007). For JPL-2011b, the PPP solutions used ECMWF/VMF1 products, but the GIPSY orbit and clock products at the time used GPT2 products, which reflect annual and semi-annual fits to monthly mean ECMWF weather data over several years (Boehm et al. 2007; Lagler et al. 2013). The NGL-IGS08 solutions assume static a priori zenith hydrostatic and wet delays and the Global Mapping Function (GMF), which accounts for average annual variations in atmospheric conditions from ECMWF (Boehm et al.

2006a). The JPL-2018a solutions assume the GPT2w set of a priori zenith hydrostatic and wet delays and mapping functions, which represent an update to the GPT2 model with improved estimates of zenith wet delays (Lagler et al. 2013; Boehm et al. 2015). GPT2w and GMF are both considered blind models that can be used for low-latency applications (e.g., Boehm et al. 2015); however, blind models are not as effective at capturing the true variations in the wet and dry troposphere as full-resolution numerical weather models, such as ECMWF/VMF1.

Tropospheric parameters are further refined stochastically for all data products at sub-daily resolution during GPS antenna-position estimation to compensate for inaccuracies in numerical weather models. The wet component of the delay is associated with water vapor in the atmosphere and has relatively large fluctuations over time as well as large uncertainties (Bevis et al. 1992; Jin et al. 2014). Systematic errors commonly result during the refinement of wet delays when the a priori hydrostatic delays, which depend on surface pressure, are inaccurate (Tregoning and Herring 2006).

Another important aspect of GPS processing involves the reference frame used for coordinate estimation as well as for the satellite orbit and clock products. All of the products considered here use International GNSS Service (IGS) realizations of the International Terrestrial Reference Frame (ITRF). Three of the products (NGL-IGS08, JPL-2011b, and UNAVCO) adopt the IGS08 reference frame, whereas the remaining two products (NGL-IGS14 and JPL-2018a) adopt the updated IGS14 reference frame (Altamimi et al. 2011, 2016). We note that, since the time of our analysis, newer UNAVCO products are now available in the NAM14 and IGS14 frames.

To transform GPS network positions into an IGS frame, JPL and NGL apply scale factors to all GPS positions on each day. First, for each day, JPL pre-computes orbits and clocks of 24–32 satellites as well as positions of about 80 reference GPS sites on Earth's surface in a loosely constrained reference frame. Next, JPL and NGL generate daily PPP solutions in a non-fiducial (GIPSY v6) or no-net-rotation (GipsyX) frame and then transform the PPP solutions into an IGS frame by applying daily estimates of a rotation, translation, and scale factor (using JPL "x-files"). Applying the scale factor can increase or decrease the vertical-position estimate on a day by as much as 6 mm. The series of scale values has a peak-to-peak seasonal oscillation at Earth's surface of 3 mm with a maximum in September. In this study, JPL and NGL take the vertical position of a GPS site to be the position estimate with the scale factor applied. This represents the two institutions' best estimate of the true position of a GPS site following the IERS standards (Petit and Luzum 2010).

In contrast, the CWU (GIPSY v6) contribution to the UNAVCO solutions uses JPL non-fiducial orbit and clock products, applies a daily frame rotation and translation based on a regional-scale network of reference receivers concentrated in North America, and does not apply a scale factor. The UNAVCO solution is transformed into an IGS frame by minimizing differences at sites in North America (including Greenland, Alaska, and central America); this site distribution covers about 1/4 of Earth's surface and represents a frame intermediate between global and regional, resulting in moderate spatial filtering. Herring et al. (2016) postulate that the application of scale factors associated with the regional North America-centric frame could worsen GPS estimates of vertical position and absorb real geophysical signal of interest; thus, scale factors are not applied.

Product discrepancies are largely driven by differences in the following data-processing choices: (1) treatment of a priori zenith troposphere delay, (2) troposphere mapping function, (3) software package, and (4) reference frame. A summary of these key choices is provided in Table 1. We do not provide an exhaustive description or comparison of all data-processing choices due to the sheer number and complexity of them. Preliminary studies of product sensitivity conducted prior to reprocessing at NGL suggest that other choices are of lesser importance. These include fine tuning of integer-phase ambiguity resolution methods, pre-editing of the raw observations, post-editing of the data residuals, higher-order ionospheric corrections, elevation cutoffs of signals close to the horizon, elevation-dependent weighting, treatment of body tides and tidal ocean loading, and process noise settings for time-dependent parameters. One possible exception might be process noise settings during rare, extreme atmospheric conditions, which would go beyond the scope of this study. Note that many processing choices

Table 1 A summary of key differences in GPS data-processing strategies between analysis centers and data-product versions

	NGL	NGL	UNAVCO	JPL	JPL
	IGS14	IGS08	Early 2019	2018a	2011b
A Priori Zenith Delay	ECMWF	Static	ECMWF	GPT2w	ECMWF
Tropospheric mapping function	VMF1	GMF	VMF1	GPT2w	VMF1
Software	GipsyX	GIPSY v6	GIPSYv6+GAMIT	GipsyX	GIPSY v6
Reference frame	IGS14	IGS08	IGS08	IGS14	IGS08 (pre-2018)

are identical, given that data processing centers tend to follow community-accepted practices, such as the use of IGS antenna calibration files and IERS conventions.

2.2 Assessing time-series scatter

We post-process each of the five data products using the same set of procedures. We first identify and remove segments of data that are fewer than 60 days in length and separated from other data by at least 60 days, since isolated data segments are sometimes associated with equipment malfunction. We then remove offsets from the time series associated with known earthquakes and equipment changes using a catalog of events and offset amplitudes provided by the UNAVCO consortium (Herring et al. 2016). All known offsets larger than 8 mm and 4 mm in the vertical and horizontal components, respectively, are removed. For coseismic offsets that produced at least 40 mm of displacement, we also fit and remove a postseismic-deformation signal using a logarithmic decay model that characterizes afterslip (e.g., Kreemer et al. 2006). We allow both the relaxation time and decay amplitude to be determined directly from the data via a least-squares inversion. Experimenting with an exponential-decay model, which may better characterize viscoelastic flow, yielded comparable RMS error relative to the logarithmic-decay model.

We then identified and removed outliers from each time series using a running median absolute deviation filter with a median window of 30 days and a median absolute deviation threshold of a factor of 10. The filter evaluates the absolute deviations of GPS positions away from the running median and determines whether individual positions exceed the median value of all absolute deviations multiplied by the threshold factor. Furthermore, we exclude stations that recorded fewer than 730 days of data within the 3-year study period (October 1, 2012, through October 1, 2015).

We next fit and remove a mean position, velocity, and sinusoid with a period of one year from the data; we make the fits separately for each spatial component (east, north, up) at each station. Although atmospheric loading exhibits some seasonal variation in the contiguous USA and Alaska (cf. Fig. 2), most of the seasonal signal is dominated by hydrologic loading; thus, we include an annual sinusoid. We use linear (unweighted) least-squares regression to find the best fit of the following model to each time series:

$$y(t) = a + b\,t + c\cos(\omega t) + s\sin(\omega t) \quad (1)$$

where t is time in days and ω represents the angular frequency of a harmonic signal with a period of one year ($\omega = 2\pi/365$ days). The unknown coefficients a and b define the constant and linear-trend terms, and the unknown coefficients c and s together characterize the amplitude and phase of seasonal deformation. An annual sinusoid is fit and removed from the data unless otherwise specified (e.g., for exploration of seasonal oscillations; discussed later).

Total root-mean-square (RMS) scatter provides a means to assess the overall quality of the five solutions. We define RMS scatter as the RMS error relative to a long-term mean displacement of zero, because all of the post-processing cor-

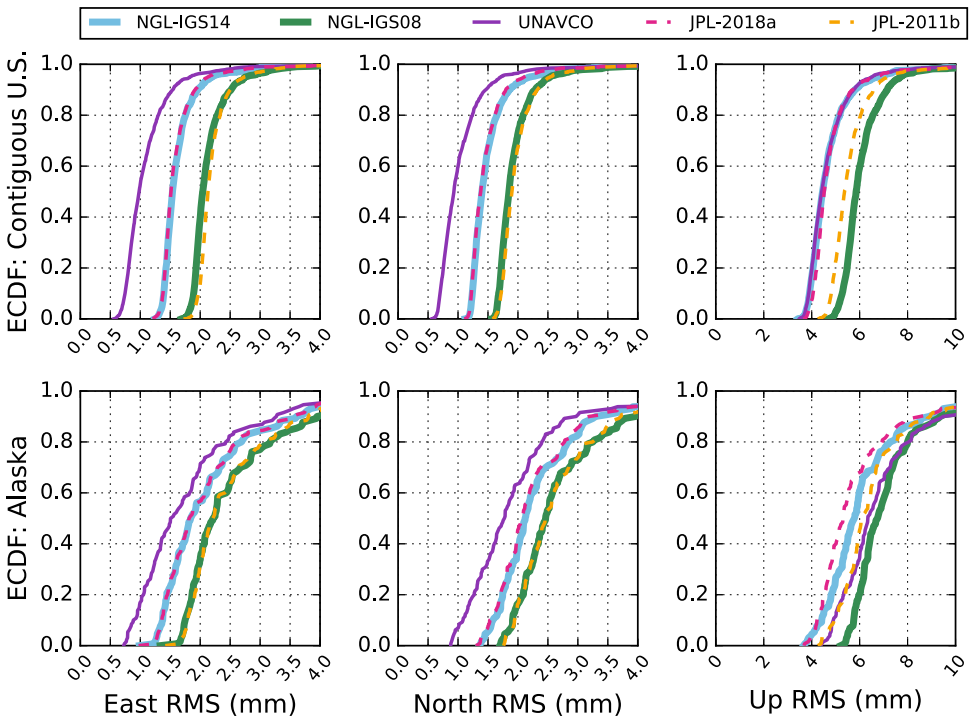

Fig. 1 Empirical cumulative distribution functions (ECDFs) of time-series scatter prior to the application of atmospheric-loading corrections. The RMS scatter is computed relative to a mean position (averaged over three years), a velocity, and an annual sinusoid, estimated individually for each component of each station. Offsets and outliers have also been removed. The top panels correspond to GPS data collected in the contiguous USA (south of 50° latitude); the bottom panels correspond to GPS stations in Alaska. The left, center, and right panels show scatter in the east, north, and up components, respectively. We compare the scatter for five GPS datasets (see legend at top): NGL-IGS14, NGL-IGS08, UNAVCO, JPL-2018a, and JPL-2011b. A total of 1185 stations common to all datasets are considered

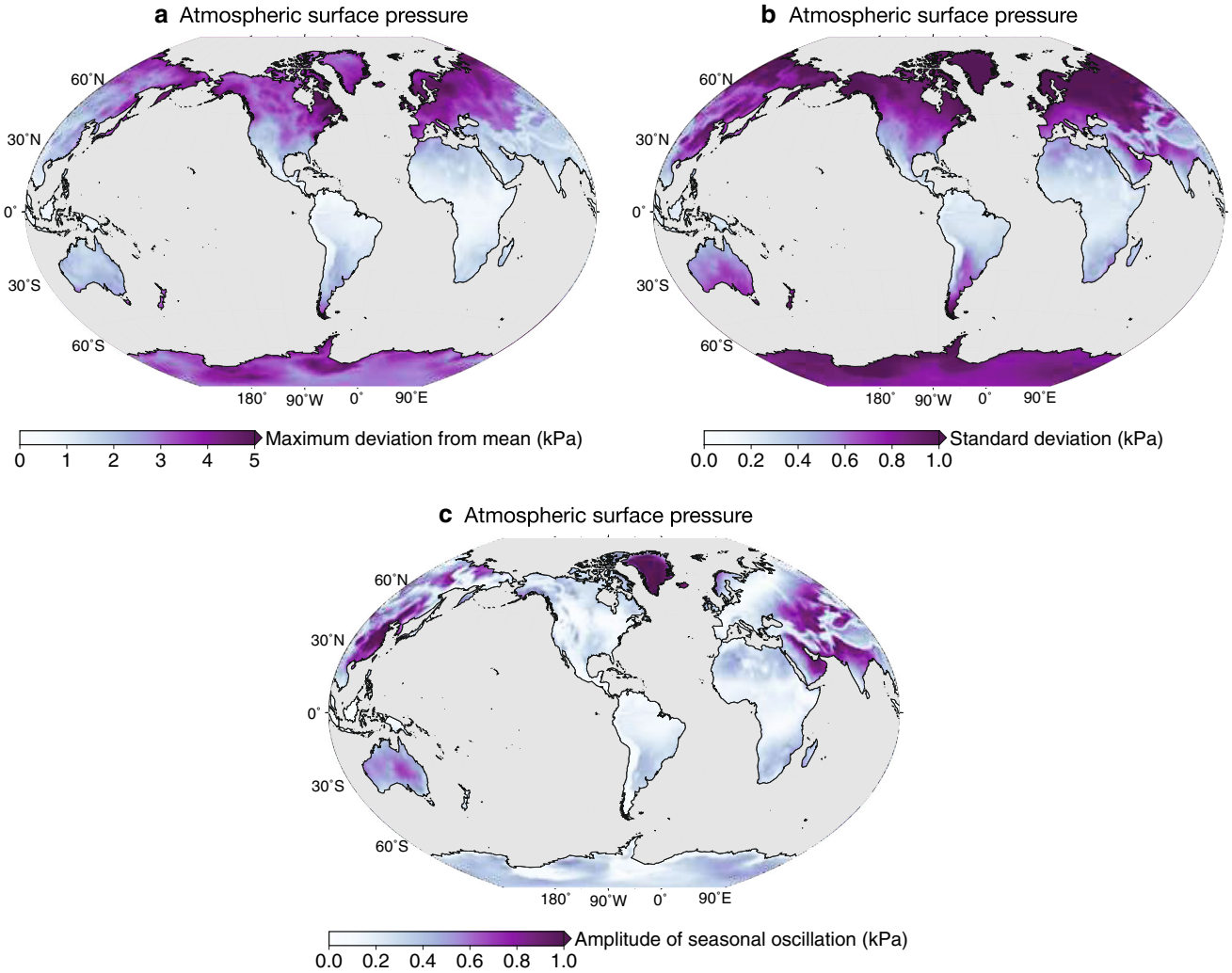

Fig. 2 Global maps of atmospheric surface-pressure anomalies for the period of 2012–2015 from the European Centre for Medium Range Weather Forecasts (ECMWF; ERA-Interim). The anomalies are computed relative to a three-year average (2012–2015), with both spatial and temporal averages removed. Plotted are: **a** maximum deviations from the mean in atmospheric surface pressure; **b** standard deviation from the mean in atmospheric surface pressure; and **c** the amplitude of seasonal oscillations (i.e., a sinusoid with a period of one year) in atmospheric surface pressure. For large pressure systems, the vertical response of the Earth to atmospheric pressure loading is roughly 0.5 mm/mbar (5 mm/kPa). Although not explored in detail here, a similar figure depicting variations in non-tidal oceanic pressure is provided in the supporting information

rections defined above (including the model described in Eq. 1) have already been applied. Figure 1 shows empirical cumulative distribution functions (ECDFs) of RMS scatter for the east-, north-, and up-component time series at 1185 GPS stations common to all data products; an ECDF value of 0.5 represents the median RMS scatter. Results are shown separately for stations located north of 50° latitude (mostly in Alaska) and stations located south of 50° latitude (mostly in the contiguous USA). RMS scatter is larger overall for the stations at higher latitude, and approximately three times larger in the up component than in the horizontal components.

The newer data products, NGL-IGS14, JPL-2018a, and UNAVCO, exhibit the lowest RMS scatter in all three displacement components, suggesting improved quality. The older NGL-IGS08 and JPL-2011b solutions consistently exhibit relatively high RMS scatter in all components and both geographic regions, suggesting poorer overall quality. The UNAVCO series exhibit the lowest RMS scatter in the horizontal components; however, this may be due to UNAVCO's use of a regional reference-frame transformation. To define the transformation, UNAVCO uses approximately 500 stations centered on North America (with coverage of about 25% of the globe), whereas both JPL and NGL use a global network of about 80 stations. Application

of a non-global reference-frame transformation is by definition a "common-mode filter," which tends to reduce RMS scatter of GPS time series, but does not necessarily improve the product. For example, removing a common-mode signal can reduce systematic errors (e.g., orbit errors), but can also absorb real geophysical signal (e.g., loading), with a net average displacement and tilt on the continental scale.

2.3 Predicting atmospheric pressure loading

The solid Earth deforms under the weight of surface mass loads in a manner governed by the material properties of Earth's interior (e.g., Longman 1962, 1963; Farrell 1972; Martens et al. 2016a). To forward-model the deformation caused by a particular load, both a model for the interior structure of the Earth as well as a model for the surface-load distribution must be given (e.g., Farrell 1973; Guo et al. 2004; Martens et al. 2019).

Determining the spatial distributions of fluid-mass transfer through time requires ongoing measurements of the Earth system at the global scale. Remote-sensing data (e.g., gravity, surface deformation, radar, altimetry) collected by space-based platforms supplement ground-based measurements to provide continual and large-scale constraints on the time-evolving state of Earth's fluid envelopes, which inform models of changes in atmosphere mass, non-tidal ocean mass, and hydrology (e.g., Fu et al. 1994; Nerem et al. 2010; Tapley et al. 2004; Stephens et al. 2008; Dee et al. 2011).

Global maps of atmospheric surface-pressure anomalies during the three-year study period are shown in Fig. 2. The largest variations in atmospheric pressure are at high latitudes, with a predominantly long-wavelength spatial distribution (e.g., van Dam et al. 1994; Herring et al. 2016). Annual variations in atmospheric pressure are relatively large in Greenland (cf. Liu et al. 2017), northern India, east Asia, and Australia, and relatively small in North and South America, western Europe, and Africa.

Solid Earth's elastic-deformation response to variations in atmospheric surface pressure varies in similar geographic fashion, and additionally depends on the proximity of the observation location to the ocean due to the "inverted-barometer" effect (e.g., van Dam et al. 1994, 1997; Wunsch and Stammer 1997; Herring et al. 2016). The inverted-barometer (IB) effect explains how ocean height changes in response to atmospheric pressure change. An increase (or decrease) in atmospheric pressure results in a drop (or rise) in sea level, such that the total pressure at the ocean bottom remains constant (Wunsch and Stammer 1997). Since the IB effect neutralizes Earth's deformation response to atmospheric pressure loading over the ocean regions, the impact of the effect diminishes in magnitude with distance inland from the coast. In the contiguous USA, the IB effect compensates for about 2 mm of vertical crustal displacement, on average, along the coasts and the magnitude of compensation diminishes to about 0.6 mm in the center of the continent (see supporting information). At approximately 400–500 km inland from either coast, the IB effect has decayed to about half its maximum value.

Here, we make use of non-tidal atmospheric loading (NTAL) models provided by the Earth System Modelling Group of GeoForschungsZentrum Potsdam (ESMGFZ) (Dill and Dobslaw 2013). The atmospheric-loading models are calculated using surface-pressure data from ECMWF, incorporating both re-analysis and operational datasets (e.g., Dee et al. 2011). Atmospheric tides are removed for 12 dominant harmonics. The surface-pressure fields are convolved with displacement load Green's functions in the center-of-figure (CF) reference frame (Blewitt 2003) derived from the ak135f Earth model (Kennett et al. 1995). Loading values are provided on a 0.5° by 0.5° regular global grid with a time resolution of 3 hours, which we interpolate to each GPS receiver location. For comparison with daily GPS solutions, we average the modeled displacement values over the course of each day.

For verification, we cross-check the ESMGFZ models against models of atmospheric loading computed by an independent load-deformation modeling software, `LoadDef` (Martens et al. 2019). Over the three-year study period, differences between the models are predominantly less than 0.3 mm in the vertical component and less than 0.1 mm in the horizontal components (see supporting information). Small differences are expected for a few reasons: ESMGFZ removes atmospheric tidal constituents, but LoadDef does not; LoadDef computes load-induced displacements at the location of each receiver directly, whereas ESMGFZ provides global grids of displacement that require interpolation to each station location; and ESMGFZ models are computed from several ECMWF products (ERA-40, ERA-Interim, and operational ECMWF), whereas the LoadDef models are computed from ECMWF ERA-Interim products. Furthermore, slight differences in model baseline can arise due to discrepancies in the time-averaged atmospheric-pressure response removed from each model.

3 Atmospheric loading corrections

3.1 Reduction in scatter of GPS vertical positions when atmospheric pressure loading is removed

We next explore the extent to which atmospheric pressure loading can explain scatter in residual GPS time series, which may otherwise be interpreted as "noise." We compute changes in RMS scatter when correcting residual time series for atmospheric loading. Assessments of changes in RMS

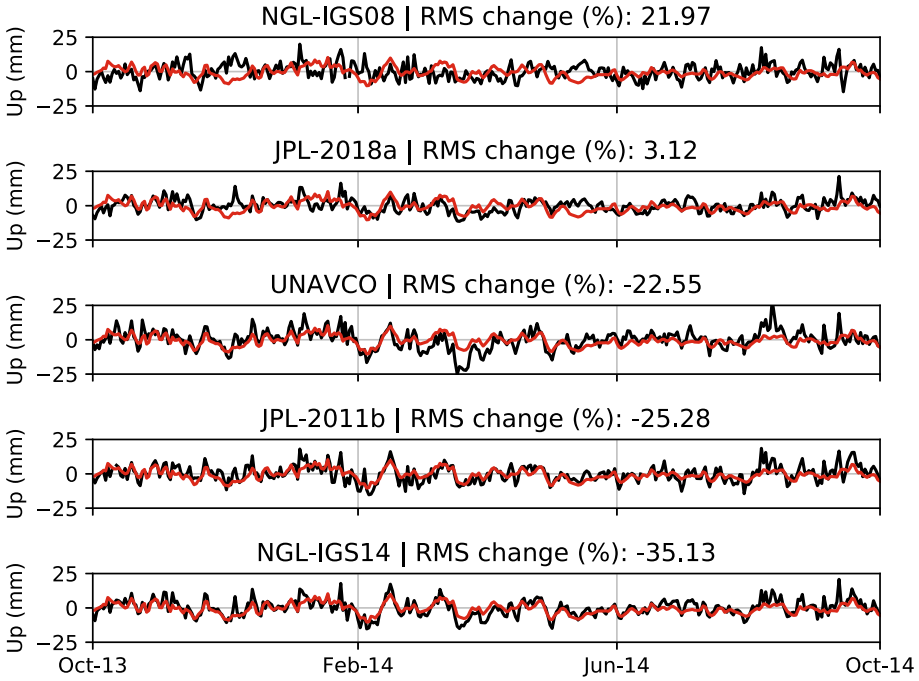

Fig. 3 Up-component GPS-inferred displacement time series (black lines) for station AB15 in Alaska and the period from October 1, 2013, to October 1, 2014. The time series are based on five different data products, from top to bottom (in order of poorest to best reduction in scatter): NGL-IGS08, JPL-2018a, UNAVCO, JPL-2011b, and NGL-IGS14. Daily estimates of non-tidal atmospheric pressure loading are overlaid as red lines. The atmospheric loading model is the same in each panel. The change in root-mean-square scatter is quoted at the top of each panel as a percentage; a negative value indicates a reduction in time-series scatter after the application of NTAL corrections

scatter are made with respect to residual time series generated using the data-reduction methods described in Sect. 2.2.

As an example, Fig. 3 shows up-component time series from PBO station AB15 in Alaska for each of the five data products over a one-year period from 1 Oct 2013 through 1 Oct 2014. The atmospheric-loading model, interpolated to the geographic location of AB15 from the ESMGFZ grids, is overlaid in red (and identical in each panel). RMS scatter is reduced for only three of the five data products after applying atmospheric-loading corrections: NGL-IGS14, UNAVCO, and JPL-2011b. All three products use high-resolution troposphere delays based on numerical weather models (i.e., ECMWF zenith delays and VMF1 mapping functions) during processing. For NGL-IGS14, 35% of the scatter in the residual time series can be explained by NTAL. For JPL-2011b and UNAVCO, 25% and 23% of the scatter in the residual time series, respectively, can be explained by NTAL. In contrast, the JPL-2018a and NGL-IGS08 solutions, which both use approximate and slowly varying troposphere-delay models, exhibit increases in time-series scatter (by +3% for JPL-2018a and +22% for NGL-IGS08). Although the older JPL-2011b series use high-resolution VMF1 products, the newer JPL-2018a series use the lower-resolution GPT2w troposphere models in order to guarantee the availability of troposphere models at low latency.

Figure 4 depicts changes in RMS scatter for the up components of GPS series across the contiguous USA; results for Alaska are shown in Fig. 5. Here, we consider the full three-year study period: 1 Oct 2012 through 1 Oct 2015. The figures show all available stations for each data product, which vary by product; statistics are based on a subset of 1185 stations common to all products. The reductions in RMS scatter are most pronounced for the NGL-IGS14 (−6.2% median reduction in the contiguous USA and −15.2% in Alaska) and UNAVCO (−9.1% in contiguous USA and −15.1% in Alaska) solutions. Maximum reductions in RMS scatter exceed −40% at some stations when considering NGL-IGS14 and UNAVCO solutions, indicating that up to 40% or more of residual time-series scatter can be explained by NTAL in certain regions (mostly at higher latitudes and in the central USA). The JPL-2011b solutions also yield significant reductions in RMS scatter (−5.2% median reduction in the contiguous USA and −10.9% in Alaska).

The NGL-IGS08 and JPL-2018a solutions, on the other hand, yield systematic increases in RMS scatter, particularly within several hundreds of kilometers of the Pacific coast (Fig. 4). For each of the five data products, reductions in up-component RMS scatter improve toward the center of the continent, which is due in part to the inverted-barometer effect of the oceans. Spatial variations in RMS-scatter reduction also reflect spatial variations in regional weather patterns and associated atmospheric-pressure fluctuations, which affect the size of the atmospheric-loading signal. Central and eastern parts of the USA exhibit larger fluctuations in atmospheric surface pressure over time relative to the western USA (Fig. 2). Another potential contribution to improved scatter reductions in the central USA may be spatial variations in the background noise levels of the GPS time series; reductions in RMS scatter depend not only on the size of the signal being removed, but also on the background noise. Noise levels may be higher in the western USA due to tectonic activity and strong variations in topography that cannot

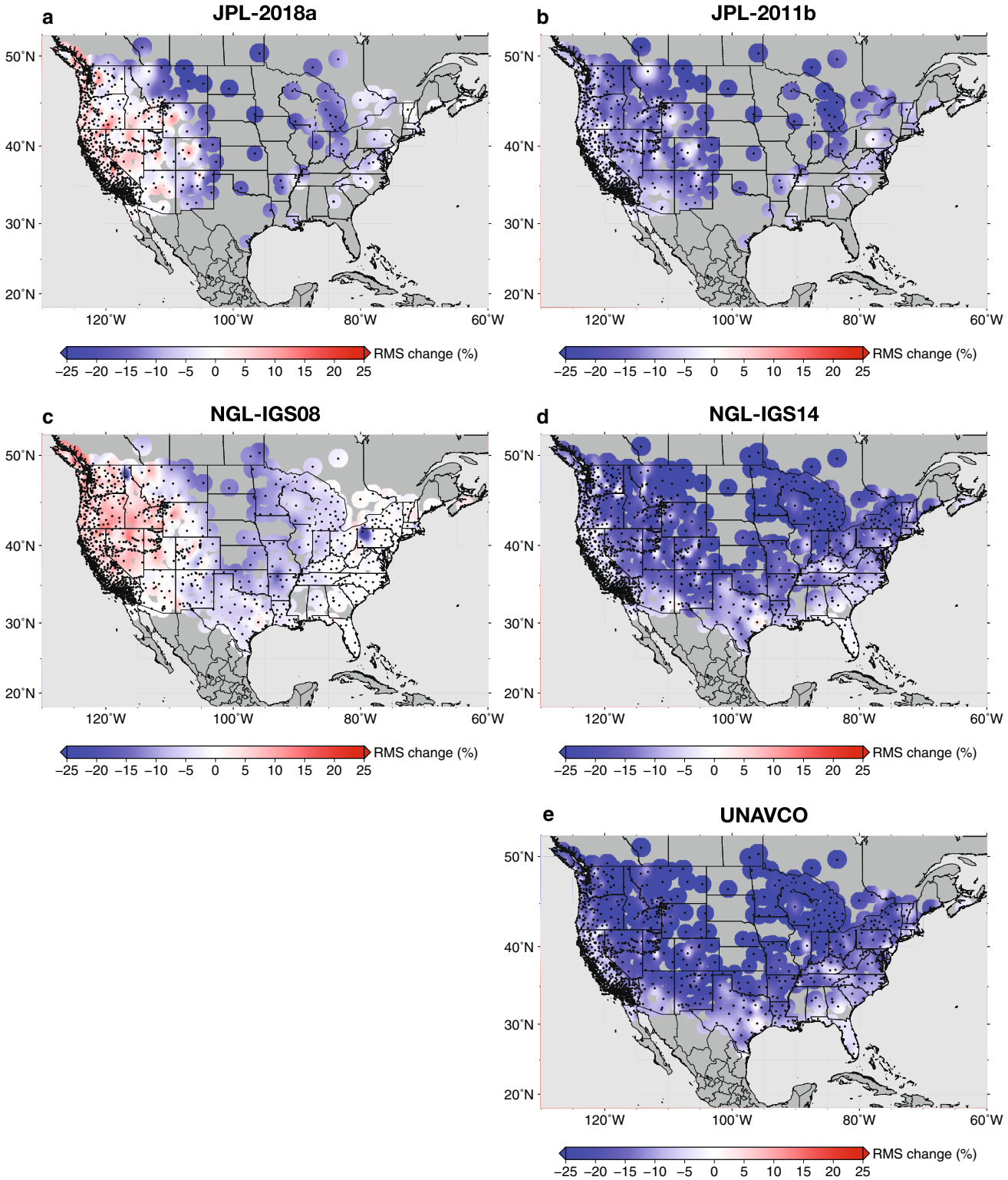

Fig. 4 Percent changes in root-mean-square scatter in the up component of GPS series when NTAL corrections are applied for the time period from October 1, 2012, to October 1, 2015. The change in scatter is small and mostly positive for GPS solutions that use static/GMF and GPT2w troposphere-delay models (left-hand column). JPL-2018a and NGL-IGS08 yield median increases in RMS scatter of +1.9% [−1.0%, +4.0%] and +3.3% [+0.9%, +5.2%], respectively. The values in brackets reflect the 25% and 75% quartiles of the scatter changes. The reduction in scatter is relatively large for GPS solutions that use high-resolution ECMWF/VMF1 troposphere-delay models (right-hand column): median RMS decrease of −5.2% [−9.4%, −2.9%] for JPL-2011b, −6.2% [−11.8%, −3.1%] for NGL-IGS14, and −9.1% [−15.7%, −5.6%] for UNAVCO. For the computations of median RMS, we limit the computation to a total of 1054 stations in the contiguous USA that are common to all data products. Individual panels show all available stations for each data product

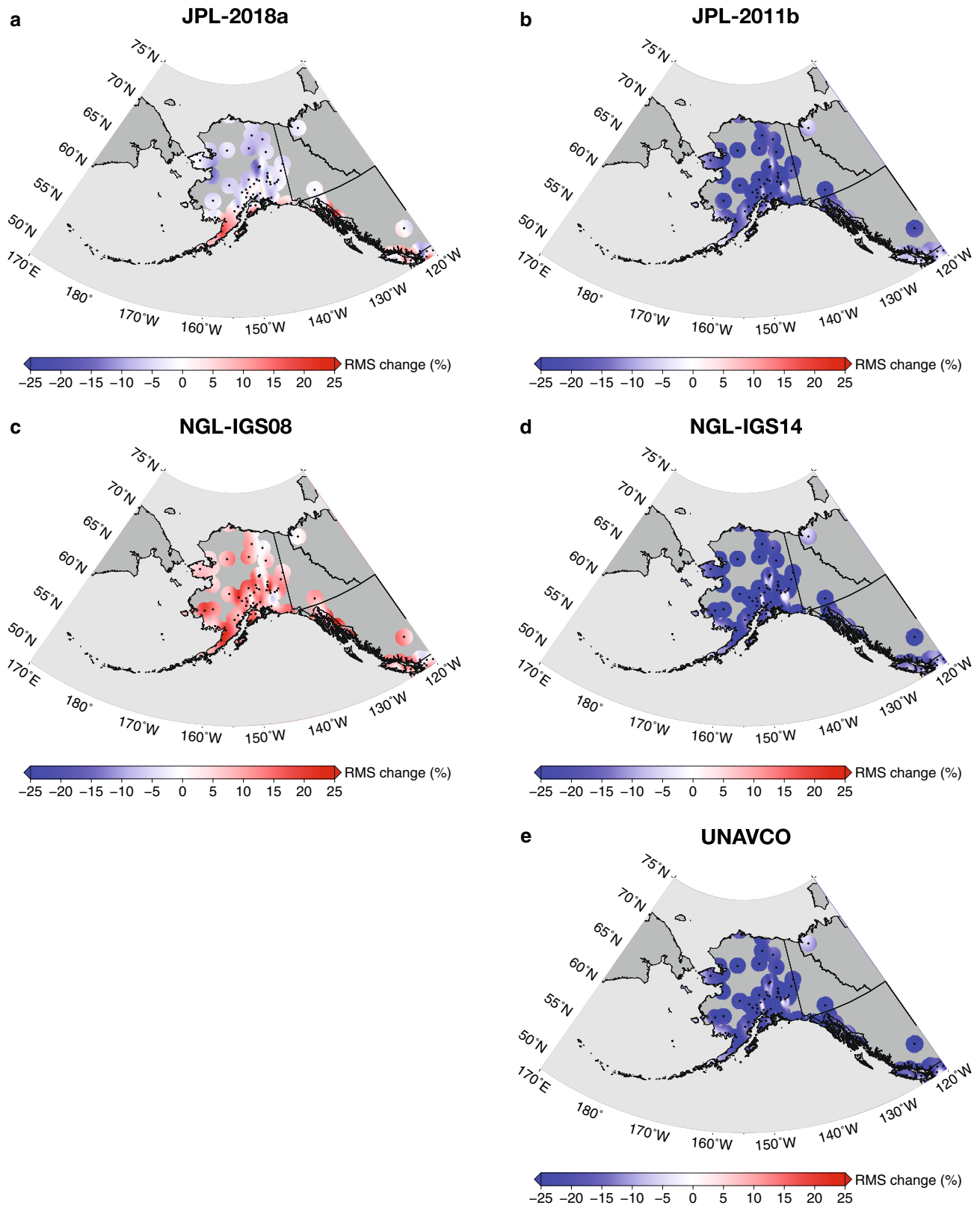

Fig. 5 Same as Fig. 4, but for stations in Alaska. Median changes in RMS scatter are +7.6% [+3.6%, +12.1%], +0.9% [−2.8%, +5.7%], −10.9% [−20.3%, −5.7%], −15.2% [−26.8%, −8.4%], and −15.1% [−25.7%, −7.7%] for the NGL-IGS08, JPL-2018a, JPL-2011b, NGL-IGS14, and UNAVCO series, respectively. The values in brackets reflect the 25% and 75% quartiles of the scatter changes. For the computations of median RMS, we limit the computation to a total of 131 stations in Alaska that are common to all data products. Individual panels show all available stations for each data product

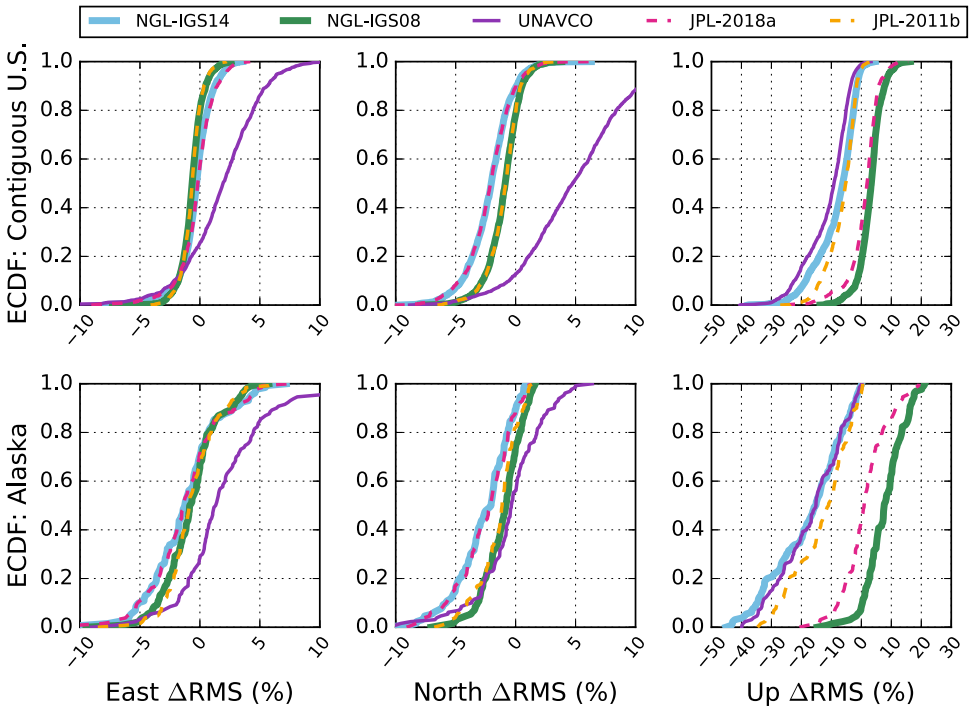

Fig. 6 Empirical cumulative distribution functions (ECDFs) of percent changes in RMS scatter in the east (left), north (center), and up (right) components of GPS series when NTAL (ESMGFZ models; CF frame) is removed over the time period from October 1, 2012, to October 1, 2015. The top panels represent the changes in RMS scatter for PBO stations south of 50° latitude (primarily within the contiguous USA), and the bottom panels represent the changes in RMS scatter for PBO stations north of 50° latitude (primarily in Alaska). We compare changes in RMS scatter after removing the same NTAL model from five GPS datasets: NGL-IGS14, NGL-IGS08, UNAVCO, JPL-2018a, and JPL-2011b. We consider a total of 1185 stations common among all datasets

be fully captured by the spatial resolution of the NTAL models.

Figure 6 summarizes the changes in RMS scatter, after applying corrections for NTAL, as empirical cumulative distribution functions (ECDFs). Changes in RMS scatter tend to be larger at high latitudes, where fluctuations in atmospheric surface pressure are also large (Fig. 2). GPS solutions derived using simplified troposphere-delay models (NGL-IGS08 and JPL-2018a) consistently yield either poor reductions in up-component RMS scatter or increases in RMS scatter after NTAL corrections are applied. Since mismodeled troposphere delays have been shown to absorb part of the atmospheric-loading signal from GPS time series (e.g., Steigenberger et al. 2009), the sub-optimal changes in RMS scatter exhibited by NGL-IGS08 and JPL-2018a indicate that the removal of NTAL at the post-processing stage (e.g., using the ESMGFZ suite of NTAL models) can overcorrect for the effects of atmospheric loading and degrade the accuracy of the time series.

The apparent relationship between the accuracy of troposphere-delay models and the reduction in RMS scatter after applying NTAL corrections suggests that the high-resolution ECMWF/VMF1 models produce the most precise GPS site positions, relative to the blind and approximate GPT2w, GMF, and static-delay models. Our results are consistent with prior studies that found that high-resolution troposphere delays based on empirical data yield smaller GPS height errors and produce time series that better retain the atmospheric-loading signal (e.g., Tregoning and Herring 2006; Boehm et al. 2006a; Steigenberger et al. 2009; Munekane and Boehm 2010).

We verify the results at additional stations (over 3500) and with longer data records (over a decade) for the NGL-IGS08 and NGL-IGS14 time series. Reductions in up-component scatter after applying NTAL corrections are shown in Fig. 7. Correcting for NTAL substantially reduces scatter for the NGL-IGS14 products (median reductions of -7% in the western USA and -14% in the eastern USA), but not for the NGL-IGS08 products (no reduction in scatter across most of the contiguous USA).

Although our present analysis focuses primarily on the effects of NTAL corrections, ESMGFZ also provides models for non-tidal oceanic loading based on the MPIOM ocean general circulation model (Dill and Dobslaw 2013). Reductions in up-component scatter after removing both non-tidal atmospheric and oceanic loading across the contiguous USA are shown in the supporting information. Based on comparison with Fig. 7, changes in time-series scatter are dominated by the effects of NTAL; non-tidal oceanic loading has a relatively minor effect (mostly $<1\%$) and is not investigated further here. ESMGFZ also supplies models of hydrologic mass loading, which is known to dominate the seasonal displacement signal in North America (e.g., Argus et al. 2014; Fu et al. 2015; Argus et al. 2017). Here, we emphasize the effects of NTAL on daily GPS positions, but explore the impacts of GPS data processing and NTAL corrections on estimates of seasonal deformation in Sect. 5.

We acknowledge that reductions in RMS scatter do not necessarily accurately characterize the extent to which GPS

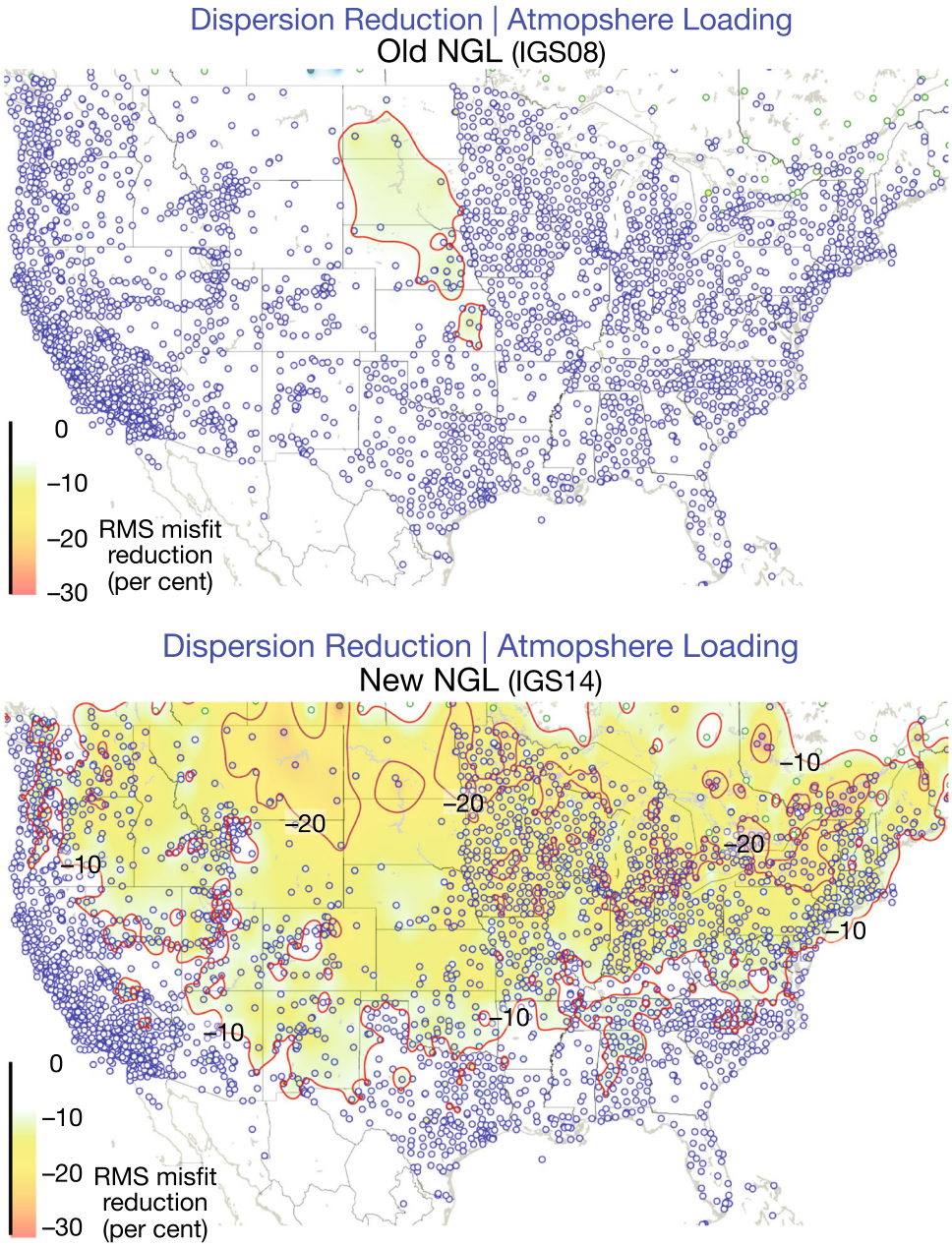

Fig. 7 Percent changes in RMS scatter in the up component of 3500 GPS series in the USA when NTAL is removed from GPS positions starting around 2006 and ending in 2019. The change in scatter is nearly zero for NGL-IGS08 (top diagram), which uses the GMF troposphere model (median RMS scatter decrease of 1%). The reduction in scatter is significant for NGL-IGS14 (bottom diagram), which corrects for the ECMWF/VMF1 troposphere model (median RMS scatter decrease of 12%). The median reduction in RMS scatter for the NGL-ISG14 series is slightly larger here than in Fig. 4 (12% vs 6%) due to the inclusion of more stations in the central USA, where Earth deformation caused by NTAL is greater

"noise" can be explained by atmospheric loading. For two signals in a time series that destructively interfere, correcting for one of the signals increases the RMS scatter, even when the unwanted signal has been perfectly removed (e.g., Tregoning and Watson 2009, Sect. 3). However, most geophysical signals that contribute significantly to geodetic time series (e.g., semi-diurnal and diurnal ocean tides, seasonal hydrologic deformation, long-term plate motions and glacial isostatic adjustment) do not vary consistently at the same rate as atmospheric surface pressure, which fluctuates predominantly on daily to weekly timescales. The magnitude of atmospheric loading generally exceeds other signals relevant to daily position estimates that might vary over similar periods (e.g., non-tidal oceanic loading). Furthermore, we compute scatter reductions over long time intervals (a minimum of 3 years) so as to limit the likelihood of systematic destructive interference between atmospheric loading and other unmodeled signals in the time series. Systematic errors associated with estimates of surface pressure may still persist (e.g., errors may differ systematically between high- and low-pressure weather systems, which have different capacities for moisture and precipitation).

3.2 Reduction in scatter of GPS horizontal positions when atmospheric pressure loading is removed

We also consider the effects of GPS processing and NTAL corrections on the horizontal-displacement time series. Figure 8 depicts the changes in RMS scatter for north-component time series in the contiguous USA; east-component changes and results for Alaska are shown in the supporting information. Changes in RMS scatter are significantly smaller in the horizontal components than in the up component. Furthermore, changes in RMS scatter for the horizontal components show different spatial patterns and different relationships with data products than for the up component. The NGL-IGS14 and JPL-2018a solutions yield modest, albeit systematic and relatively large, reductions in north-component RMS scatter (−2.0% median reduction in both the contiguous USA and Alaska). In contrast, the UNAVCO solutions exhibit systematic and relatively large increases in RMS scatter after applying NTAL corrections to the horizontal components (+4.7% median increase for the north component in the contiguous USA), which likely relates to the use of a regional reference frame. We postulate that a portion of the NTAL may have been absorbed into the regional transformation parameters; thus, the application of NTAL corrections increases RMS scatter. Notwithstanding, the UNAVCO horizontal series exhibit the lowest RMS scatter to begin with (Sect. 2.2), which is also due in part to spatial filtering associated with the regional reference frame. Even with the small increase in scatter after applying NTAL corrections, the UNAVCO horizontal series have lower total RMS scatter than the other data products (cf. Fig. 1).

Changes in RMS scatter for the horizontal components are small in comparison with the vertical components, but appear to be spatially coherent (Fig. 8), which suggests that the RMS changes are not random. The small-magnitude changes in RMS scatter for the horizontal components (Fig. 6), relative to the up component, are consistent with prior studies that found simplified troposphere delays to have relatively little effect on the horizontal coordinate positions (e.g., Tregoning and Herring 2006; Kouba 2009).

We postulate that the horizontal components may be particularly sensitive to the choice and consistency of reference frame between the forward models and observations, which might contribute to the relatively large increases in RMS scatter for the UNAVCO horizontal series. The UNAVCO solutions are unique among the five data products in not adopting the JPL x-file transformations. Sensitivities of horizontal displacements to inconsistent reference frames between forward models and observations have also been seen in analyses of Earth's response to ocean tidal loading (e.g., Fu et al. 2012; Martens et al. 2016b).

3.3 Relationships between troposphere delays and atmospheric loading

From comparisons of five GPS data products (Fig. 6), we find that height time series derived using the ECMWF/VMF1 troposphere-delay models consistently yield the largest reductions in RMS scatter after applying NTAL corrections, relative to time series derived using simplified troposphere-delay models (e.g., GPT2w, GMF, static delay). Our results provide empirical evidence, based on a large and spatially dense network of GPS stations, that high-resolution troposphere-delay models (e.g., ECMWF/VMF1) yield more precise GPS position estimates that best retain the NTAL signal. Time series derived from accurate, high-resolution troposphere-delay models are therefore well suited for the application of high-resolution NTAL corrections during post-processing (e.g., ESMGFZ). Time series derived from approximate, low-resolution troposphere-delay models run the risk of being degraded by NTAL corrections applied during post-processing.

Our results are consistent with prior studies that have demonstrated how mismodeled (low accuracy and/or low temporal resolution) troposphere delays absorb part of the atmospheric-loading signal (e.g., Tregoning and Herring 2006; Kouba 2009; Steigenberger et al. 2009). The partial compensation relates to the negative correlation between zenith hydrostatic delays and atmospheric loading: a higher atmospheric pressure corresponds to an increased zenith hydrostatic delay (in units of distance) and a greater downward displacement of the GPS station due to atmospheric loading (Steigenberger et al. 2009). If the fluctuations in the zenith hydrostatic delays are systematically underestimated relative to the true fluctuations, which is common when delays are approximated by spatial and temporal smoothing of high-resolution numerical weather models (e.g., GPT2w models are derived from monthly mean ECMWF data), then fluctuations in GPS heights can also be underestimated relative to the true heights (Steigenberger et al. 2009). Although uncommon (because mismodeled delays generally occur due to deliberate spatial and temporal smoothing), it is theoretically possible for fluctuations in the zenith hydrostatic delays to be overestimated relative to the true fluctuations; in this case, the atmospheric loading signal could be artificially amplified rather than damped.

The use of incorrect zenith hydrostatic and wet delays inhibits the ability of the mapping functions to accurately characterize the delays for satellite elevation angles close to the horizon as well as to estimate corrections to the a priori delays over time (Tregoning and Herring 2006). Errors in the zenith hydrostatic delays can be particularly problematic when only wet mapping functions are used to compute time-varying correction factors for both the zenith hydrostatic and wet delays (Tregoning and Herring 2006), which

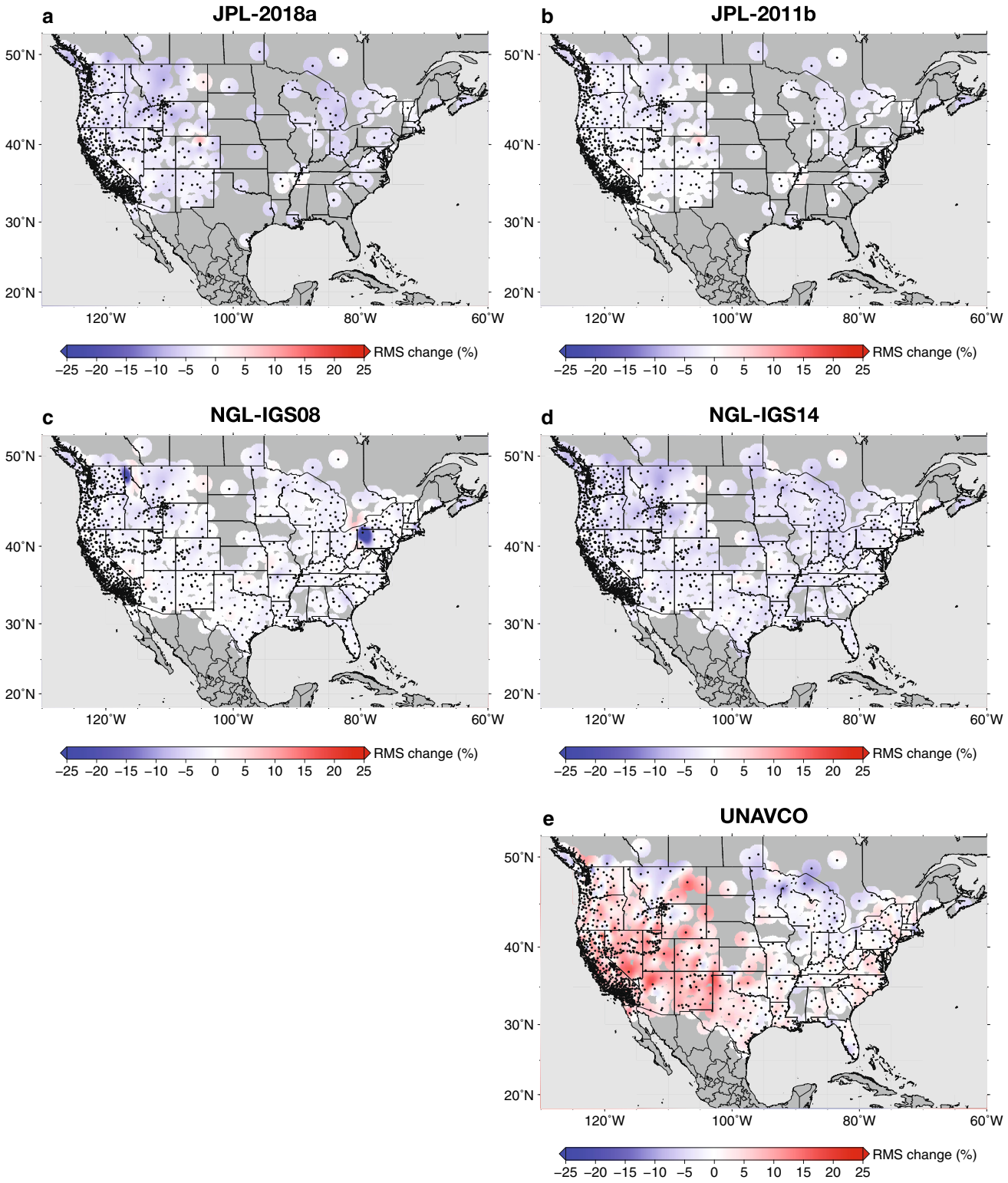

Fig. 8 Percent changes in RMS scatter in the north component of GPS series when NTAL corrections are applied for the time period from October 1, 2012, to October 1, 2015. Changes in RMS scatter for the east component, as well as for both horizontal components in Alaska, are shown in the supporting information. To facilitate direct comparison with Fig. 4, we have kept the order of datasets the same; however, in the horizontal components, UNAVCO yields the largest increases in RMS scatter after applying NTAL corrections. The individual panels show all available stations for each data product

is common practice because the wet delays usually vary much more than the hydrostatic delays. Discrepancies between the modeling of wet and hydrostatic delays produce errors in the GPS position estimates that result in the partial removal of Earth movement caused by atmospheric loading.

Tregoning and Herring (2006) and Kouba (2009) show that the degree of compensation depends upon the magnitude of the error in the a priori zenith hydrostatic delay, the weighting of satellite signals by elevation, and the elevation-angle cutoff for signals near the horizon, with lower elevation-angle cutoffs resulting in a larger absorption of atmospheric loading. Errors introduced by mismodeled troposphere delays can be particularly pronounced at high latitudes, where most of the incoming satellite signals arrive lower to the horizon (Tregoning and Herring 2006). Similar effects on ocean tidal loading have also been reported: approximate, low-resolution troposphere delays and improperly tuned process-noise settings to model stochastic troposphere fluctuations can lead to the absorption of high-frequency tidal signals (e.g., Khan and Scherneck 2003; Penna et al. 2015; Martens et al. 2016b).

4 Correlations between common GPS data products

Figure 9 shows ECDFs of Pearson correlation coefficients between several pairs of GPS time series from the three processing centers considered in our analysis (NGL, JPL, and UNAVCO). We remove a mean position, velocity, and a sinusoid with a period of one year from each time series prior to computing the correlations, but do not apply atmospheric-loading corrections. Correlations between time series with NTAL corrections applied, which exhibit similar trends, are shown in the supporting information. The Pearson correlation coefficient (PCC) provides a measure of the linear relationship between two time series: a coefficient of 1 indicates a perfect positive linear relationship; a coefficient of -1 indicates a perfect negative linear relationship; and a coefficient of 0 indicates a perfect absence of a linear relationship. Ideally, all of the data products would correlate perfectly with each other (and be independently accurate) after initial position estimation and the application of corrections for known signals; in practice, the data products exhibit notable differences.

We find that the NGL-IGS14 and JPL-2018a solutions (both without and with NTAL removed) yield the highest correlations among all product pairs, indicating a strong positive linear relationship between the two time series, despite the different treatment of troposphere delays during processing. The NGL-IGS14 and JPL-2018a solutions represent relatively recent analyses generated using an updated realization of a global reference frame (IGS14) with identical implementation (i.e., JPL non-fiducial orbit and clock products and the same transformation parameters). Furthermore, NGL-IGS14 and JPL-2018a both use the GipsyX software, which limits differences in processing. NGL-IGS14 and JPL-2018a also have among the lowest total RMS scatter in the vertical-component time series (Fig. 1), indicating enhanced precision relative to older products. NGL-IGS14 and JPL-2018a products are thus similar in most regards, with the exception of the treatment of troposphere delay (Table 1). Since troposphere delay and atmospheric loading are correlated, differences between the time series are more pronounced in comparisons of time-series scatter reductions after applying NTAL corrections (e.g., Fig. 4). Spatial relationships among correlation coefficients are shown in the supporting information.

5 Effects of GPS processing on estimates of seasonal deformation

To evaluate the effects of GPS processing and NTAL corrections on estimates of seasonal deformation (often attributed to annual fluctuations in continental water storage), we compare three-component annual deformation estimated from the five data products across the contiguous USA and Alaska. We first apply standard corrections to each time series based on the methods described in Sect. 2.2, albeit without fitting and removing an annual harmonic a priori. We next apply NTAL corrections using the ESMGFZ models averaged over each day, which are based on surface-pressure fields from ECMWF (Sect. 2.3). Amplitudes and phases of annual deformation are then estimated empirically using Eq. 1 for each spatial component at each station.

Figure 10 shows seasonal deformation in the western USA estimated from the NGL-IGS14 and UNAVCO GPS solutions. We depict the seasonal motion at each station by a particle motion ellipse (PME) (cf. Martens et al. 2016b). The size, shape, and orientation of each PME depict horizontal seasonal motion. When deformation is caused by mass loading, the semi-major axes of the PMEs align in the direction of maximum seasonal loading and unloading. The color of each PME depicts vertical seasonal amplitude (i.e., half the total peak-to-peak range of the oscillation). Figure 10c shows the vector differences between seasonal displacements estimated from the NGL-IGS14 and UNAVCO solutions, which we refer to as "residual PMEs"; median differences exceed 1 mm amplitude in the vertical component. The seasonal and residual PMEs vary at the same period (annual) in all three spatial components; thus, the PMEs are closed in three-dimensional space.

Nearly all of the residual PMEs across the western USA exhibit a systematic northeast-southwest alignment (i.e., NE-SW orientation of PME semi-major axes at most stations), which cannot be related to local site effects. Removing a

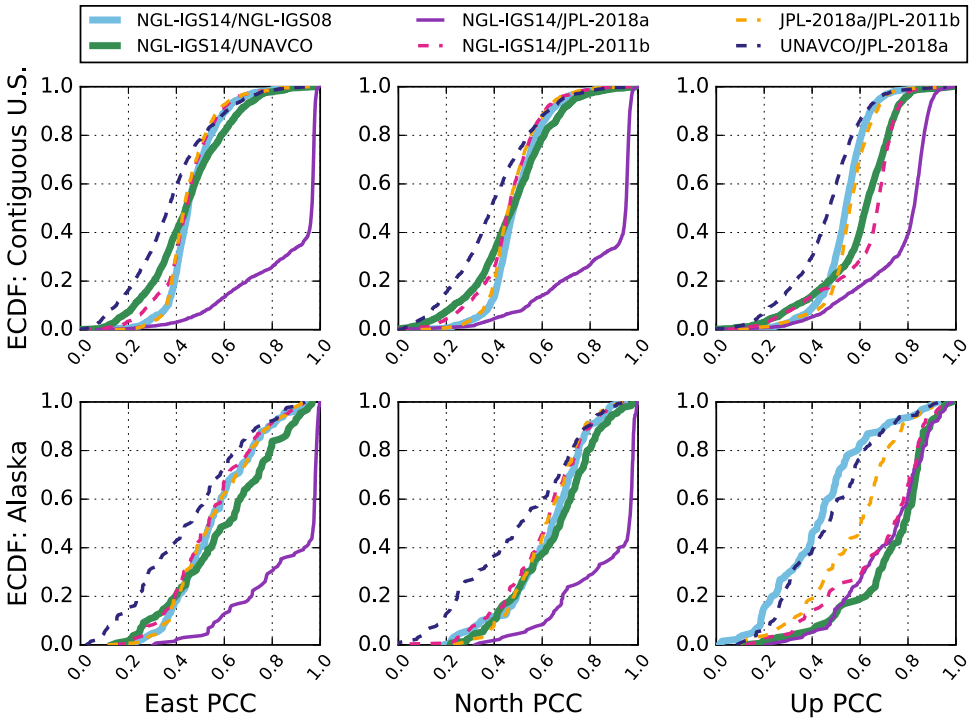

Fig. 9 Empirical cumulative distribution functions showing Pearson correlation coefficients between selected pairs of GPS data products. A mean position, velocity, and annual sinusoid have been removed from each time series prior to computing the correlations; atmospheric-loading corrections have not been applied. PCCs for pairs of time series with atmospheric-loading corrections applied yield similar patterns and are shown in the supporting information

network-averaged seasonal amplitude and phase from each spatial component at each station, which we call the "seasonal common mode," reduces the seasonal-deformation residuals between the two data products by 30–80% (median reductions) in all three spatial components (Fig. 10d; see also Fig. 12). We suggest that the discrepancies stem in large part from different reference-frame realizations (i.e., global IGS14 for NGL-IGS14 and regional IGS08 for UNAVCO). The seasonal common mode, which exhibits harmonic motion with a period of one year in all three spatial components, may also be represented by a PME (shown in the lower-left corner of Fig. 10d). We emphasize that the seasonal common mode described here, which characterizes a constant seasonal amplitude and a constant seasonal phase common to all stations (computed separately for each spatial component), should not be confused with a network-averaged displacement at each time epoch removed from a geodetic time series.

Figure 11 is identical to Fig. 10, but compares seasonal deformation estimated from the NGL-IGS14 and JPL-2018a solutions. The residual PMEs in this comparison also exhibit a network-coherent pattern, albeit far less pronounced than for the comparison between NGL-IGS14 and UNAVCO. In contrast with Fig. 10, both NGL-IGS14 and JPL-2018a use the same parameters (translation, rotation, and scale) to transform the position series into the IGS14 reference frame and both use the GipsyX software. The vector differences in seasonal deformation between NGL-IGS14 and JPL-2018a are predominantly less than 1 mm amplitude in the up component (Fig. 11c), and reduced further to differences of about 0.5 mm amplitude after removing the seasonal common mode (Fig. 11d). Comparisons of seasonal PMEs for additional data products and for stations in Alaska are shown in the supporting information.

A summary of vector differences in seasonal deformation for pairs of data products is shown in Fig. 12. Most seasonal residuals, *after* removing the seasonal common mode, fall within the range of 0.1–0.3 mm amplitude in the horizontal components and 0.4–1.0 mm amplitude in the up component (Fig. 12). The discrepancies in estimated seasonal deformation are broadly consistent with previous investigations into the effects of GPS processing methods on estimates of seasonal deformation: Tregoning and Herring (2006) found that GPS height errors associated with inaccurate troposphere delays could generate discrepancies in seasonal amplitude of up to about 2 mm, particularly in high-latitude regions.

We find that seasonal deformation derived from UNAVCO solutions exhibits relatively large differences in the contiguous USA with respect to the other data products, but that the large differences display network coherency and can be substantially reduced (by two- or three-fold) by removing a seasonal common mode. We suggest that the large differences in estimates of seasonal deformation between UNAVCO and other products stem largely from inconsistencies in reference-frame realization (e.g., optional use of scale factors and the spatial extent of reference networks). Furthermore, UNAVCO combines antenna-position estimates from two processing centers that use different orbit and clock prod-

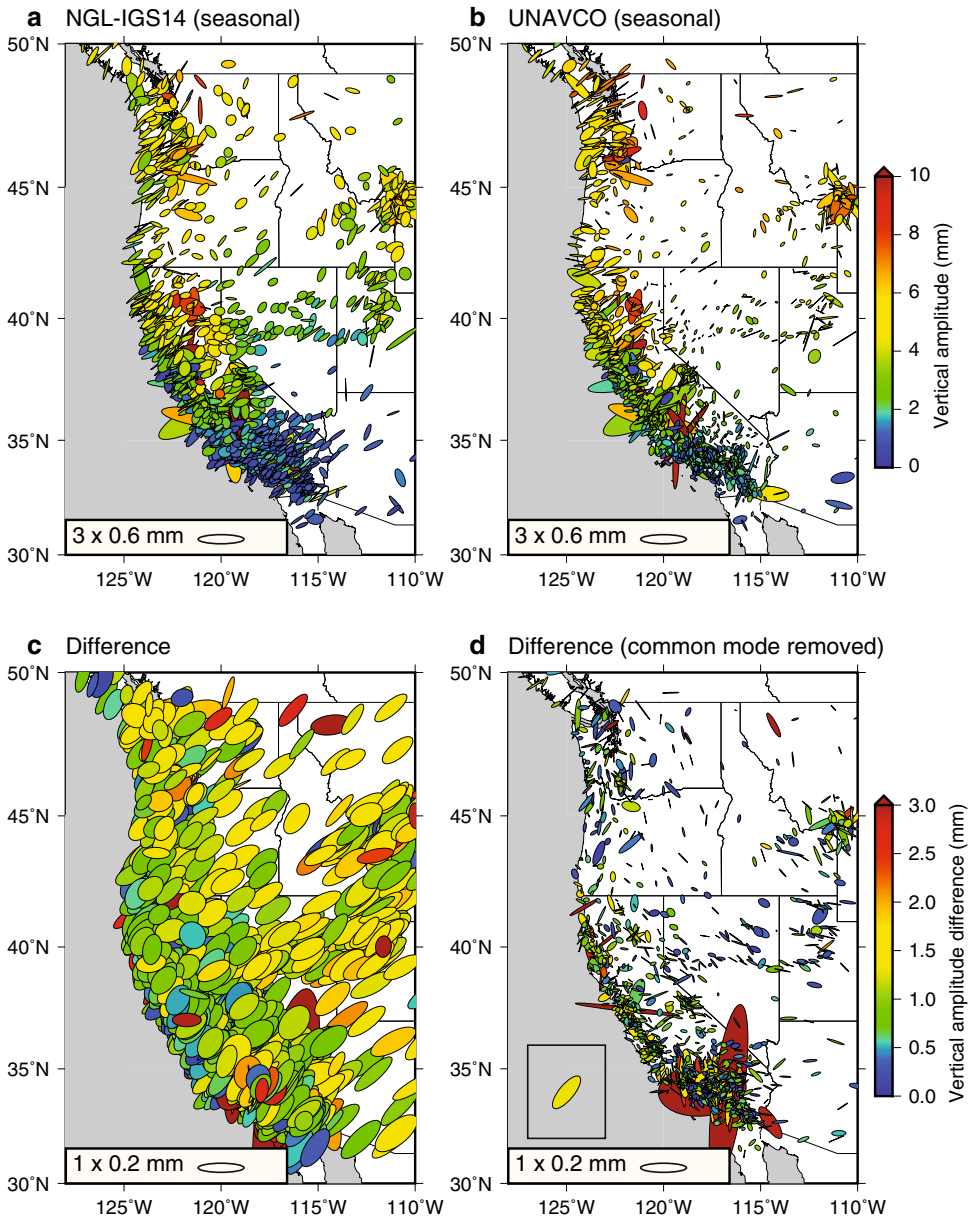

Fig. 10 Seasonal oscillations in **a** NGL-IGS14, **b** UNAVCO, and **c** their vector differences for the time period from October 1, 2012, to October 1, 2015. Panel (**d**) shows the vector differences in estimated seasonal deformation after a seasonal common mode has been removed. The seasonal oscillations are depicted by particle motion ellipses (PMEs), which illustrate the seasonal horizontal motion of each GPS site (reference ellipse at bottom left shows size; numeric values quote amplitude, which is half the total peak-to-peak oscillation); the vertical amplitude of the seasonal oscillation is given by the color of the ellipse (see colorbars). Each PME is centered on the location of a GPS site. Note that vertical- and horizontal-amplitude scales (colorbars and reference PMEs, respectively) for panels (**a**) and (**b**) differ from those in panels (**c**) and (**d**). The seasonal common mode, removed from each station in panel (**c**) to obtain the results in panel (**d**), is shown as the boxed PME in panel (**d**). In each panel, we only depict stations that are common to both data products

ucts (JPL vs IGS) and different software packages (GIPSY v6 and GAMIT) (Herring et al. 2016); for the horizontal series, the NMT and CWU contributions are about equal in the combination.

To assess the discrepancies between data products as a percentage of the magnitude of seasonal deformation, we compute the percent difference between seasonal signals estimated from pairs of data products, separately for each station and spatial component (see supporting information). The percent difference quantifies the magnitude of the vector difference between two seasonal signals relative to the average magnitude of the two signals. Median percent differences generally fall within the range of about 10–40% (after removal of the seasonal common mode) for all three spatial components. Prior to removing the seasonal common mode, some discrepancies between estimated seasonal amplitudes can exceed the average amplitude of the seasonal signal (percent differences >100%). Much of the discrepancy prior to removing the seasonal common mode can be attributed to network-coherent signal, which likely consists of long-wavelength reference-frame errors rather than true geophysical deformation.

Median percent differences of up to about 40% suggest that GPS-inferred estimates of seasonal water-storage variations could be discrepant by a factor of 1.5 or more depending on the GPS data product used to constrain the inversion. Wrongly characterizing changes in water volume could have serious implications for water-resource manage-

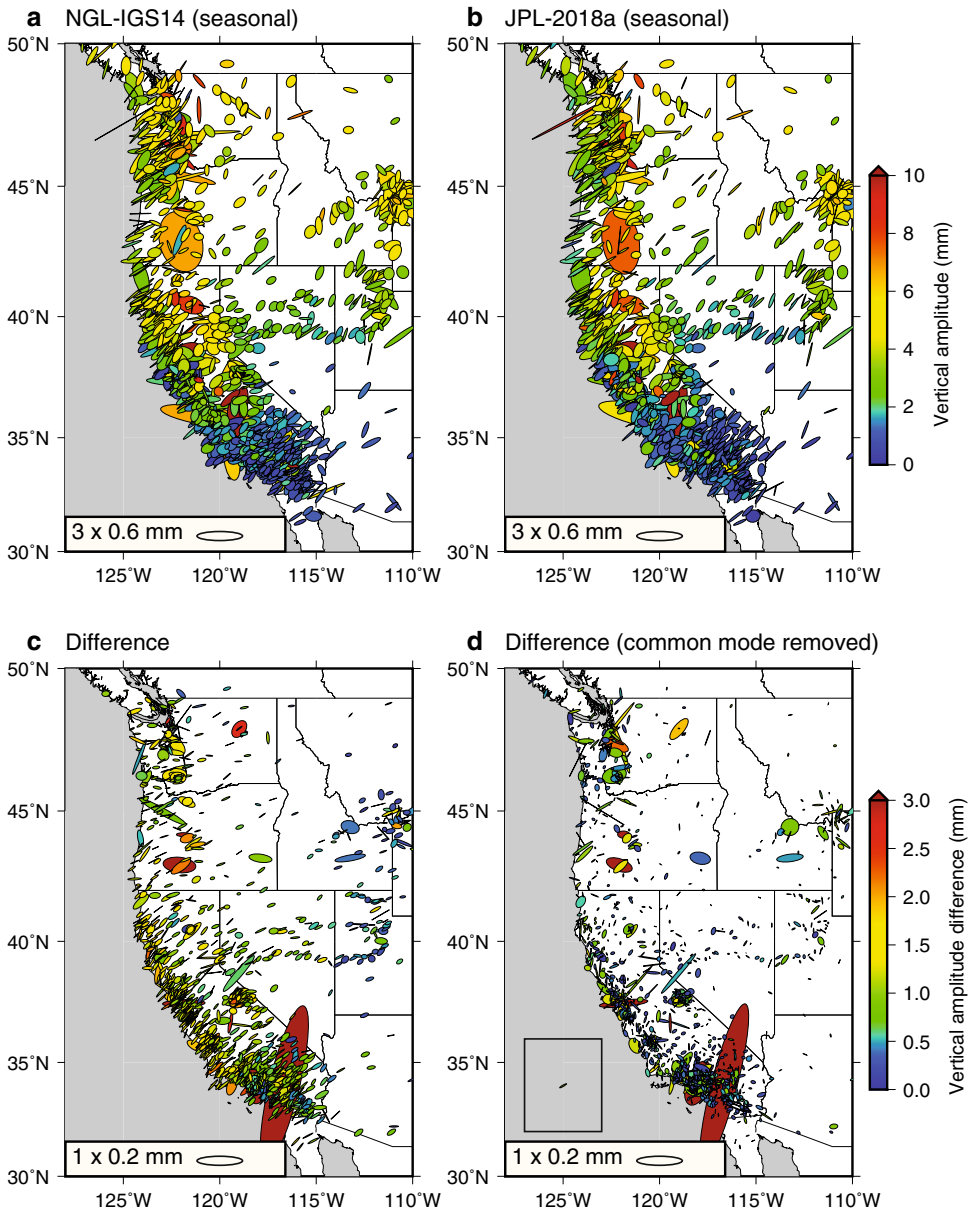

Fig. 11 Same as Fig. 10, but for the seasonal oscillations of **a** NGL-IGS14 and **b** JPL-2018a. Estimates of seasonal deformation and the differences between additional data products, including for the Alaska region, are shown in the supporting information

ment as geodesy becomes an increasingly utilized tool for monitoring hydrologic processes. Nevertheless, correlations between time series and estimates of total RMS scatter suggest that newer time series (e.g., NGL-IGS14, JPL-2018a) have improved in precision relative to older time series (e.g., NGL-IGS08, JPL-2011b). Thus, the newer data products are likely to better reflect the true seasonal oscillations, implying median relative errors of less than about 30–40%.

Since atmospheric surface pressure and loading fluctuate primarily on hourly to weekly timescales, estimates of seasonal deformation from GPS time series remain largely unaffected by mismodeled day-to-day fluctuations in troposphere and NTAL due to the separation in frequency space. The inaccurate modeling of troposphere delays and the improper application of NTAL corrections likely have larger impacts on estimates of water-mass loading at shorter periods, such as from atmospheric rivers and hurricanes. Furthermore, annual variations in atmospheric surface pressure are relatively small in the contiguous USA and Alaska (Fig. 2) and therefore have less effect on estimates of seasonal ground displacements than in other regions of the world.

We note that deformation of the Earth generated by atmospheric loading generally varies smoothly across regional GPS networks. Spatiotemporal filtering techniques applied to GPS data can therefore also be effective at removing NTAL signals and network-coherent errors (e.g., Wdowinski et al. 1997; Dong et al. 2006; Tian and Shen 2016). Spatiotemporal filtering methods, however, have difficulty

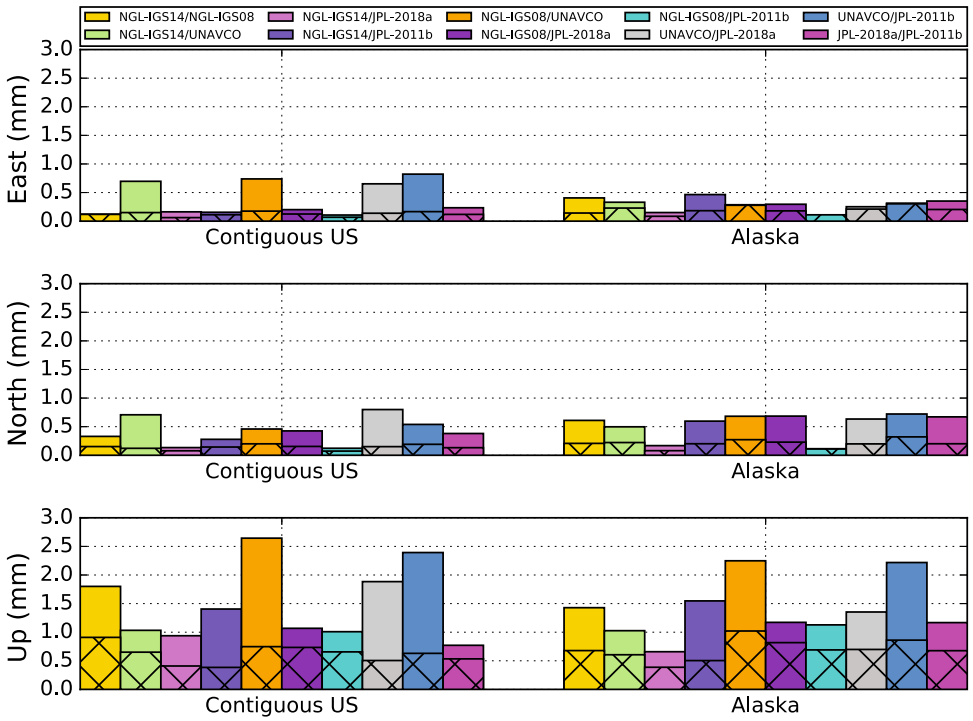

Fig. 12 Median vector differences in seasonal-oscillation amplitude estimated from pairs of five GPS data products (see legend): NGL-IGS14, NGL-IGS08, UNAVCO, JPL-2018a, and JPL-2011b. The hashing on the bars indicates the median vector differences after the seasonal common mode (network-averaged seasonal amplitude and phase) has been removed from each station. Each spatial component is treated separately in the common-mode computation

discriminating among the different nature of signals in a time series that exhibit network coherency; network-coherent changes in water mass (for example) might be unintentionally removed by spatiotemporal filters. In contrast, estimating and removing known, albeit unwanted, signals explicitly from a GPS time series can mitigate the risk for inadvertently absorbing a desired signal (e.g., deformation caused by fluctuations in water storage). Nevertheless, spatiotemporal filtering techniques may be a preferred alternative method for correcting time series produced using simplified troposphere delays (e.g., GMF, GPT2w) for the effects of NTAL because removing explicit daily NTAL predictions could overcorrect for NTAL and degrade the time series (see supporting information). With time, implementation of high-resolution troposphere delays in GPS processing is expected to become more commonplace, which would obviate the need for special treatment of NTAL corrections.

6 Summary and conclusions

We compare five GPS data products produced by three processing centers: the Nevada Geodetic Laboratory, the Jet Propulsion Laboratory, and the UNAVCO Consortium. Each of the products was derived using different processing strategies and parameter assumptions. Although we do not attempt to isolate all of the differences in processing, we highlight some of the main differences, including the treatment of radio-signal propagation delays through the troposphere and realization of reference frame. We find that newer data products (NGL-IGS14, JPL-2018a, and UNAVCO) exhibit lower total RMS scatter than older products (NGL-IGS08 and JPL-2011b), which provides evidence for improved GPS precision with newer products. The UNAVCO series have particularly low scatter in the GPS horizontal components because of the regional reference-frame realization (Fig. 1). We also find strong linear correlations between the NGL-IGS14 and JPL-2018a series, which largely reflects the use of the same software package (GipsyX) and similar parameterizations, including the reference-frame realization.

When correcting height time series for NTAL, the GPS data products derived using accurate, high-resolution troposphere delays (i.e., NGL-IGS14, UNAVCO, and JPL-2011b using ECMWF/VMF1) yield the greatest reductions in RMS scatter. Data products derived using static or slowly varying troposphere delays (i.e., NGL-IGS08 and JPL-2018a using GMF and GPT2w, respectively) are found to yield poor reductions in RMS scatter, or even significant increases in RMS scatter. We therefore recommend the use of high-resolution troposphere delays based on accurate numerical weather models (e.g., ECMWF/VMF1) during initial GPS data processing, whenever possible, in order to yield the most precise position estimates. Approximate troposphere delays (e.g., static-delay, GMF, GPT2w) absorb part of the NTAL signal, and correcting for NTAL at the post-processing stage can degrade the time series by way of an overcorrection for NTAL. Changes in RMS scatter in the horizontal compo-

nents are less pronounced than in the up component and a relationship with troposphere delays, if any, is not clear.

The slowly varying troposphere models (GPT2w, GMF) compensate primarily for day to day fluctuations in atmospheric pressure loading and have less effect on seasonal atmospheric loading (since the troposphere models vary with that period). Seasonal atmospheric fluctuations are relatively small in the contiguous USA and Alaska, with larger fluctuations elsewhere, such as in Australia and Greenland (Fig. 2).

To continue accommodating a wide array of possible scientific applications and in recognition of the indeterminate nature of numerical weather models, we do not recommend that GPS software packages implement NTAL corrections as standard procedure during processing. We recommend that NTAL corrections continue to be applied at the post-processing stage with care taken to remain consistent with the troposphere-delay modeling used during processing.

Differences in GPS processing methods also affect estimates of seasonal crustal deformation, which are associated (in part) with seasonal fluctuations in terrestrial water storage. In the contiguous USA and Alaska, differences in seasonal deformation derived from different GPS data products can exceed 0.5 mm amplitude in the horizontal components and 2.5 mm amplitude in the up component. We find that the residuals are markedly reduced after accounting for network-uniform seasonal displacements, which are likely related to reference-frame inconsistencies. After removing a seasonal common mode, differences in the amplitudes of seasonal deformation between all GPS data products generally range from 0.1–0.3 mm in the horizontal components and 0.4–1.0 mm in the up component. The discrepancies between data products provide a constraint on the precision of estimated seasonal deformation, and thus on uncertainties in inferred terrestrial water-storage variations, but should be considered in the context of the relative accuracy of each GPS data product.

As the application of GPS to infer changes in total water storage widens, improving the accuracy of GPS positioning becomes more important. Where timeliness requirements allow, high-resolution troposphere delay models using sub-daily or daily values of atmospheric surface pressure that are obtained from numerical weather models constrained by empirical data (such as ECMWF/VMF1) should be used in GPS data processing.

Acknowledgements We are grateful to Paul Ries for determining satellite orbits and clocks in JPL Repro 3.0, the basis of JPL's and NGL's latest solutions analyzed herein. Michael Heflin contributed to determining JPL's GPS solutions and creating the new GipsyX software. We gratefully acknowledge the insightful feedback from two anonymous reviewers, reviewer Adrian Borsa, and the associate editor, which strengthened the manuscript. Part of this research is performed at Jet Propulsion Laboratory, California Institute of Technology, under contract with NASA.

Author contributions H.R.M. and D.F.A. conceptualized and designed the study; H.R.M., D.F.A., and C.N. performed the formal analysis and investigation; G.B., W.C.H., and C.K. developed GPS data products and provided processing information from the Nevada Geodetic Laboratory; T.A.H. developed GPS data products and provided processing information from UNAVCO; and A.W.M. developed GPS data products and provided processing information from the Jet Propulsion Laboratory. All authors contributed to the interpretation of data and modeling results. H.R.M. wrote the first draft of the manuscript; all authors commented on this version of the manuscript. All authors read and approved the final manuscript.

Funding UNAVCO products used here are based on services provided by the GAGE Facility, operated by UNAVCO, Inc., with support from the National Science Foundation (NSF) and the National Aeronautics and Space Administration (NASA) under NSF Cooperative Agreement EAR-1724794. This research is funded in part by a NASA GNSS Remote Sensing Science Team Grant (NNH14ZDA001N-GNSS) and a NASA Earth Surface and Interior Grant (NNH18ZDA001N-ESI). Research at the University of Montana was additionally funded in part by NASA Earth Surface and Interior Grant 80NSCC19K0361 and NASA Project NNX15AK40A through the Montana Space Grant Consortium. Research at University of Nevada, Reno, was funded by NASA Earth Surface and Interior Grant 80NSSC19K1044. GB, WCH, and CK also received support from NASA Project NNX16AK89G.

Availability of data and material GPS position series are available from the Nevada Geodetic Laboratory at http://geodesy.unr.edu/gps_timeseries/, from the Jet Propulsion Laboratory (*post-point* series) at https://sideshow.jpl.nasa.gov/pub/JPL_GPS_Timeseries/, and from UNAVCO at https://www.unavco.org/data/gps-gnss/derived-products/derived-products.html. Elastic displacements produced by changes in non-tidal atmospheric loading (as well as non-tidal oceanic and hydrologic loading) are available from GFZ German Research Centre for Geosciences at https://www.gfz-potsdam.de/en/esmdata/loading and at ftp://esmdata.gfz-potsdam.de/LOADING. The LoadDef software for modeling load-induced deformation is available from Martens et al. (2019).

References

Altamimi Z, Collilieux X, Métivier L (2011) ITRF2008: an improved solution of the International Terrestrial Reference Frame. J Geod 85(8):457–473

Altamimi Z, Rebischung P, Métivier L, Collilieux X (2016) ITRF2014: a new release of the International Terrestrial Reference Frame modeling nonlinear station motions. J Geophys Res Solid Earth 121(8):6109–6131

Argus DF, Fu Y, Landerer FW (2014) Seasonal variation in total water storage in California inferred from GPS observations of vertical land motion. Geophys Res Lett 41(6):1971–1980

Argus DF, Landerer FW, Wiese DN, Martens HR, Fu Y, Famiglietti JS, Thomas BF, Farr TG, Moore AW, Watkins MM (2017) Sustained water loss in California's mountain rangesduring severe drought from 2012 to 2015 inferred fromGPS. J Geophys Res SolidEarth 122(12):10559–10585

Bertiger W, Desai SD, Haines B, Harvey N, Moore AW, Owen S, Weiss JP (2010) Single receiver phase ambiguity resolution with GPS data. J Geod 84(5):327–337

Bertiger W, Bar-Sever Y, Dorsey A, Haines B, Harvey N, Hemberger D, Heflin M, Lu W, Miller M, Moore AW et al (2020) GipsyX/RTGx, a new tool set for space geodetic operations and research. Adv Space Res 66(3):469–489

Bevis M, Businger S, Herring TA, Rocken C, Anthes RA, Ware RH (1992) GPS meteorology: remote sensing of atmospheric water vapor using the Global Positioning System. J Geophys Res Atmos 97(D14):15,787–15,801

Blewitt G (2003) Self-consistency in reference frames, geocenter definition, and surface loading of the solid Earth. J Geophys Res 108(B2):2103. https://doi.org/10.1029/2002JB002082

Blewitt G, Hammond W, Kreemer C (2018) Harnessing the GPS data explosion for interdisciplinary science. Eos 99:1–2

Boehm J, Niell A, Tregoning P, Schuh H (2006a) Global Mapping Function (GMF): a new empirical mapping function based on numerical weather model data. Geophys Res Lett 33(L07304):1–4. https://doi.org/10.1029/2005GL025546

Boehm J, Werl B, Schuh H (2006b) Troposphere mapping functions for GPS and very long baseline interferometry from European Centre for Medium-Range Weather Forecasts operational analysis data. J Geophys Res Solid Earth 111(B02406):1–9. https://doi.org/10.1029/2005JB003629

Boehm J, Heinkelmann R, Schuh H (2007) Short note: a global model of pressure and temperature for geodetic applications. J Geod 81(10):679–683

Boehm J, Moeller G, Schindelegger M, Pain G, Weber R (2015) Development of an improved empirical model for slant delays in the troposphere (GPT2w). GPS Solut 19(3):433–441

Borsa AA, Agnew DC, Cayan DR (2014) Ongoing drought-induced uplift in the western United States. Science 345(6204):1587–1590

Dee D, Uppala S, Simmons A, Berrisford P, Poli P, Kobayashi S, Andrae U, Balmaseda M, Balsamo G, Bauer P et al (2011) The ERA-Interim reanalysis: configuration and performance of the data assimilation system. Q J R Meteorol Soc 137(656):553–597

Dill R, Dobslaw H (2013) Numerical simulations of global-scale high-resolution hydrological crustal deformations. J Geophys Res Solid Earth 118(9):5008–5017

Dong D, Herring T, King RW (1998) Estimating regional deformation from a combination of space and terrestrial geodetic data. J Geod 72(4):200–214

Dong D, Fang P, Bock Y, Webb F, Prawirodirdjo L, Kedar S, Jamason P (2006) Spatiotemporal filtering using principal component analysis and Karhunen-Loeve expansion approaches for regional GPS network analysis. JGRSE 111(B03405):1–16. https://doi.org/10.1029/2005JB003806

Farrell W (1972) Deformation of the Earth by surface loads. Rev Geophys 10(3):761–797

Farrell W (1973) Earth tides, ocean tides and tidal loading. Philos Trans R Soc Lond Ser A 274(1239):253–259. https://doi.org/10.1098/rsta.1973.0050

Fu LL, Christensen EJ, Yamarone CA, Lefebvre M, Menard Y, Dorrer M, Escudier P (1994) TOPEX/POSEIDON mission overview. J Geophys Res Oceans 99(C12):24,369–24,381

Fu Y, Freymueller JT, van Dam T (2012) The effect of using inconsistent ocean tidal loading models on GPS coordinate solutions. J Geod 86(6):409–421

Fu Y, Argus DF, Landerer FW (2015) GPS as an independent measurement to estimate terrestrial water storage variations in Washington and Oregon. J Geophys Res Solid Earth 120(1):552–566

Guo J, Li Y, Huang Y, Deng H, Xu S, Ning J (2004) Green's function of the deformation of the Earth as a result of atmospheric loading. Geophys J Int 159(1):53–68. https://doi.org/10.1111/j.1365-246X.2004.02410.x

Heflin M, Donnellan A, Parker J, Lyzenga G, Moore A, Ludwig LG, Rundle J, Wang J, Pierce M (2020) Automated estimation and tools to extract positions, velocities, breaks, and seasonal terms from daily GNSS measurements: illuminating nonlinear Salton Trough deformation. Earth Space Sci 7(e2019EA000644):1–10. https://doi.org/10.1029/2019EA000644

Herring TA, Melbourne TI, Murray MH, Floyd MA, Szeliga WM, King RW, Phillips DA, Puskas CM, Santillan M, Wang L (2016) Plate Boundary Observatory and related networks: GPS data analysis methods and geodetic products. Rev Geophys 54(4):759–808. https://doi.org/10.1002/2016RG000529

Jin S, Cardellach E, Xie F (2014) GNSS remote sensing. Springer, Berlin

Kennett B, Engdahl E, Buland R (1995) Constraints on seismic velocities in the Earth from traveltimes. Geophys J Int 122(1):108–124. https://doi.org/10.1111/j.1365-246X.1995.tb03540.x

Khan SA, Scherneck HG (2003) The M2 ocean tide loading wave in Alaska: vertical and horizontal displacements, modelled and observed. J Geod 77(3–4):117–127

Kouba J (2009) Testing of global pressure/temperature (GPT) model and global mapping function (GMF) in GPS analyses. J Geod 83(3–4):199–208

Kreemer C, Blewitt G, Maerten F (2006) Co- and postseismic deformation of the 28 March 2005 Nias Mw 8.7 earthquake from continuous GPS data. Geophys Res Lett 33(L07307):1–4. https://doi.org/10.1029/2005GL025566

Lagler K, Schindelegger M, Boehm J, Krásná H, Nilsson T (2013) GPT2: Empirical slant delay model for radio space geodetic techniques. Geophys Res Lett 40(6):1069–1073

Liu L, Khan SA, van Dam T, Ma JHY, Bevis M (2017) Annual variations in GPS-measured vertical displacements near Upernavik Isstrøm (Greenland) and contributions from surface mass loading. J Geophys Res Solid Earth 122(1):677–691

Longman I (1962) A Green's function for determining the deformation of the Earth under surface mass loads: 1. Theory. J Geophys Res 67(2):845–850. https://doi.org/10.1029/JZ067i002p00845

Longman I (1963) A Green's function for determining the deformation of the Earth under surface mass loads: 2. Computations and numerical results. J Geophys Res 68(2):485–496. https://doi.org/10.1029/JZ068i002p00485

Männel B, Dobslaw H, Dill R, Glaser S, Balidakis K, Thomas M, Schuh H (2019) Correcting surface loading at the observation level: impact on global GNSS and VLBI station networks. J Geod 93(10):2003–2017. https://doi.org/10.1007/s00190-019-01298-y

Martens HR, Rivera L, Simons M, Ito T (2016a) The sensitivity of surface mass loading displacement response to perturbations in the elastic structure of the crust and mantle. J Geophys Res Solid Earth 121(5):3911–3938. https://doi.org/10.1002/2015JB012456

Martens HR, Simons M, Owen S, Rivera L (2016b) Observations of ocean tidal load response in South America from sub-daily GPS positions. Geophys J Int 205(3):1637–1664. https://doi.org/10.1093/gji/ggw087

Martens HR, Rivera L, Simons M (2019) LoadDef: A Python-based toolkit to model elastic deformation caused by surface mass loading on spherically symmetric bodies. Earth Space Sci 6(2):311–323. https://doi.org/10.1029/2018EA000462

Mémin A, Boy JP, Santamaría-Gómez A (2020) Correcting GPS measurements for non-tidal loading. GPS Solut 24(2):1–13

Milliner C, Materna K, Bürgmann R, Fu Y, Moore AW, Bekaert D, Adhikari S, Argus DF (2018) Tracking the weight of Hurricane Harvey's stormwater using GPS data. Sci Adv 4(9):1–9. https://doi.org/10.1126/sciadv.aau2477

Munekane H, Boehm J (2010) Numerical simulation of troposphere-induced errors in GPS-derived geodetic time series over Japan. J Geod 84(7):405–417

Nerem R, Chambers D, Choe C, Mitchum G (2010) Estimating mean sea level change from the TOPEX and Jason altimeter missions. Mare Geod 33(S1):435–446

Niell A (1996) Global mapping functions for the atmosphere delay at radio wavelengths. J Geophys Res Solid Earth 101(B2):3227–3246

Penna NT, Clarke PJ, Bos MS, Baker TF (2015) Ocean tide loading displacements in western Europe. Part 1: Validation of kinematic GPS

estimates. J Geophys Res Solid Earth 120(9):6523–6539. https://doi.org/10.1002/2015JB011882
Petit G, Luzum B (2010) IERS Technical Note No. 36, IERS Conventions (2010). International Earth Rotation and Reference Systems Service: Frankfurt, Germany
Petrov L, Boy JP (2004) Study of the atmospheric pressure loading signal in very long baseline interferometry observations. J Geophys Res 109(B03405):1–14. https://doi.org/10.1029/2003JB002500
Simmons A, Uppala S, Dee D, Kobayashi S (2007) ERA-Interim: new ECMWF reanalysis products from 1989 onwards. ECMWF Newsl 110:25–35
Springer A, Karegar MA, Kusche J, Keune J, Kurtz W, Kollet S (2019) Evidence of daily hydrological loading in GPS time series over Europe. J Geod 93(10):2145–2153. https://doi.org/10.1007/s00190-019-01295-1
Steigenberger P, Boehm J, Tesmer V (2009) Comparison of GMF/GPT with VMF1/ECMWF and implications for atmospheric loading. J Geod 83(10):943–951. https://doi.org/10.1007/s00190-009-0311-8
Stephens GL, Vane DG, Tanelli S, Im E, Durden S, Rokey M, Reinke D, Partain P, Mace GG, Austin R et al (2008) CloudSat mission: Performance and early science after the first year of operation. J Geophys Res Atmos 113(D00A18):1–18. https://doi.org/10.1029/2008JD009982
Tapley BD, Bettadpur S, Ries JC, Thompson PF, Watkins MM (2004) GRACE measurements of mass variability in the Earth system. Science 305(5683):503–505
Tian Y, Shen ZK (2016) Extracting the regional common-mode component of GPS station position time series from dense continuous network. J Geophys Res Solid Earth 121(2):1080–1096
Tregoning P, Herring T (2006) Impact of a priori zenith hydrostatic delay errors on GPS estimates of station heights and zenith total delays. Geophys Res Lett 33(L23303):1–5. https://doi.org/10.1029/2006GL027706
Tregoning P, Watson C (2009) Atmospheric effects and spurious signals in GPS analyses. J Geophys Res 114(B09403):1–15. https://doi.org/10.1029/2009JB006344
Tregoning P, Watson C (2011) Correction to "Atmospheric effects and spurious signals in GPS analyse". J Geophys Res 116(B02412):1–2. https://doi.org/10.1029/2010JB008157
van Dam TM, Blewitt G, Heflin MB (1994) Atmospheric pressure loading effects on Global Positioning System coordinate determinations. J Geophys Res 99(B12):23,939–23,950
van Dam T, Wahr J, Chao Y, Leuliette E (1997) Predictions of crustal deformation and of geoid and sea-level variability caused by oceanic and atmospheric loading. Geophys J Int 129(3):507–517
Wdowinski S, Bock Y, Zhang J, Fang P, Genrich J (1997) Southern California permanent GPS geodetic array: spatial filtering of daily positions for estimating coseismic and postseismic displacements induced by the 1992 Landers earthquake. J Geophys Res Solid Earth 102(B8):18,057–18,070
Wijaya DD, Böhm J, Karbon M, Kràsnà H, Schuh H (2013) Atmospheric pressure loading. In: Atmospheric effects in space geodesy. Springer, pp 137–157
Williams S, Penna N (2011) Non-tidal ocean loading effects on geodetic GPS heights. Geophys Res Lett 38(L09314):1–5. https://doi.org/10.1029/2011GL046940
Wunsch C, Stammer D (1997) Atmospheric loading and the oceanic "inverted barometer" effect. Rev Geophys 35(1):79–107
Zumberge J, Heflin M, Jefferson D, Watkins M, Webb F (1997) Precise point positioning for the efficient and robust analysis of GPS data from large networks. J Geophys Res 102(B3):5005–5017